Lagrangian transport of trace gases in the upper troposphere and lower stratosphere (UTLS)

Paul Konopka

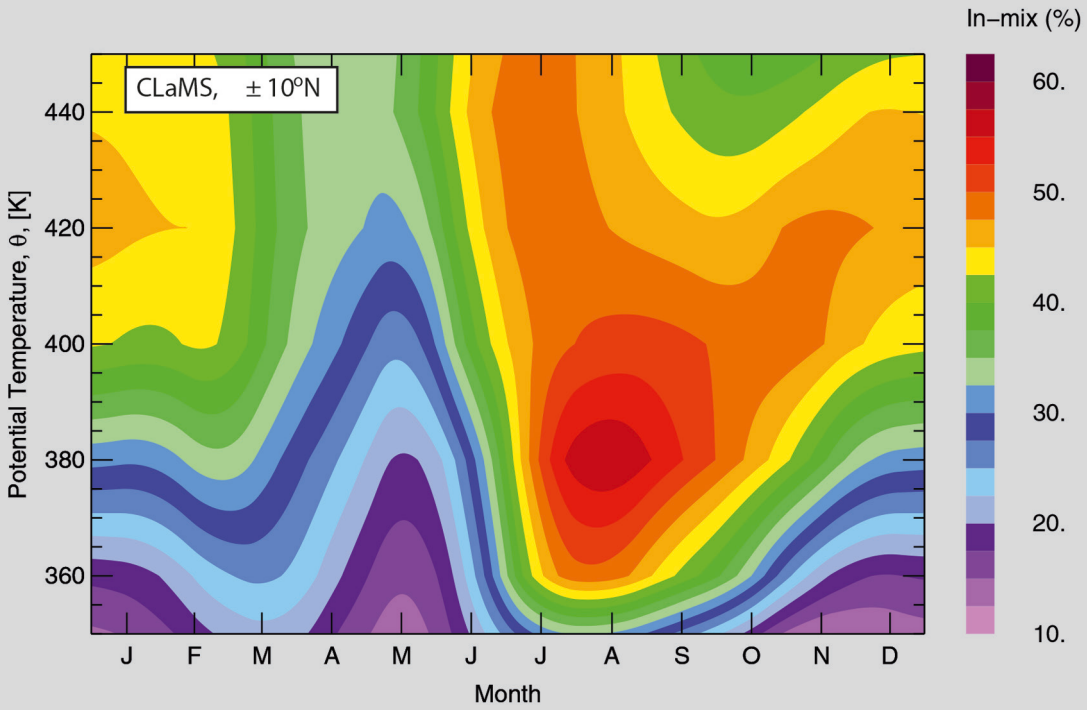

Energie & Umwelt / Energy & Environment
Band / Volume 400
ISBN 978-3-95806-279-5

Member of the Helmholtz Association

JÜLICH FORSCHUNGSZENTRUM

Schriften des Forschungszentrums Jülich
Reihe Energie & Umwelt / Energy & Environment Band / Volume 400

Forschungszentrum Jülich GmbH
Institute of Energy and Climate Research
Stratosphere (IEK-7)

Lagrangian transport of trace gases in the upper troposphere and lower stratosphere (UTLS)

Paul Konopka

Schriften des Forschungszentrums Jülich
Reihe Energie & Umwelt / Energy & Environment Band / Volume 400

ISSN 1866-1793 ISBN 978-3-95806-279-5

Bibliographic information published by the Deutsche Nationalbibliothek.
The Deutsche Nationalbibliothek lists this publication in the Deutsche
Nationalbibliografie; detailed bibliographic data are available in the
Internet at http://dnb.d-nb.de.

Publisher and Distributor: Forschungszentrum Jülich GmbH
Zentralbibliothek
52425 Jülich
Tel: +49 2461 61-5368
Fax: +49 2461 61-6103
Email: zb-publikation@fz-juelich.de
www.fz-juelich.de/zb

Cover Design: Grafische Medien, Forschungszentrum Jülich GmbH

Printer: Grafische Medien, Forschungszentrum Jülich GmbH

Copyright: Forschungszentrum Jülich 2017

Schriften des Forschungszentrums Jülich
Reihe Energie & Umwelt / Energy & Environment, Band / Volume 400

77 (Habil.-Schr., Mainz, Univ., 2015)

ISSN 1866-1793
ISBN 978-3-95806-279-5

The complete volume is freely available on the Internet on the Jülicher Open Access Server (JuSER)
at www.fz-juelich.de/zb/openaccess.

This is an Open Access publication distributed under the terms of the Creative Commons Attribution License 4.0,
which permits unrestricted use, distribution, and reproduction in any medium, provided the original work is properly cited.

Abstract

Using the Chemical Lagrangian Model of the Stratosphere (CLaMS), which was developed in the last two decades, we discuss the following, process-oriented questions: (i) how to understand the formation of the extratropical mixing layer, which separates the troposphere from the stratosphere, (ii) what is the impact of mixing processes on the tropopause inversion layer (TIL) and, finally, (iii) how to explain the large annual cycle of ozone above the tropical tropopause. Furthermore, CLaMS is also applied to understand the atmospheric long-term variability. Here, we discuss how major sudden stratospheric warmings influence stratospheric water vapor trends and how tropospheric ozone trends can be separated from the stratospheric influence. Finally, we quantify the influence of uncertainties in the understanding of atmospheric mixing on the uncertainties in radiative forcing.

The opportunity to avoid, or at least to minimize, the numerical diffusion ever present in Eulerian numerical schemes is the strongest motivation for the Lagrangian formulation of transport. We show how Lagrangian transport implemented in CLaMS goes even further and uses the numerical diffusion to parameterize physical mixing. This *kumulative Habilitationsschrift* is based on 16 studies, which are appended to the text (along with a brief description of the highlights in chapters 1 and 3), that were undertaken with the aim of improving our knowledge of various transport processes in the stratosphere and upper troposphere.

Zusammenfassung

Unter Verwendung des in den letzten zwei Jahrzehnten entwickelten chemischen Modells der Stratosphäre (CLaMS – Chemical Lagrangian Model of the Stratosphere) werden einige prozeßorientierte Anwendungen diskutiert, in denen der Lagrangesche Transport mit der reellen Atmosphäre verglichen wird. Wir gehen unter anderem der Frage nach, (i) wie man die Entstehung der extratropischen Mischungsschicht erklärt, die die Troposphäre von der Stratosphäre trennt, (ii) welchen Eif uß die Mischungsprozesse auf die Bildung der Tropopausen-Inversionschicht (TIL) haben oder aber, (iii) was die Erklärung für den augeprägten Jahresgang des Ozons oberhalb der tropischen Tropopause ist. Darüberhinaus wird auch die Langzeitvariabilität der Atmosphäre untersucht. Unter Verwendung von CLaMS zeigen wir, wie die stratosphärischen Trends von Wasserdampf durch starke Stratosphärenerwärmungen beeinf usst werden und, wie man die troposphärischen Trends von Ozon vom stratosphärischen Einf uß trennen kann.

Die stärkste Motivation für das Modellieren des Transports aus Lagrangescher Sicht ergibt sich aus der Möglichkeit, die in Eulerischen Transporschemata allgegenwertige numerische Diffusion zu vermeiden oder zumindest zu minimieren. Wir zeigen, wie der Lagrangsche Transport in CLaMS darüber hinausgeht und die numerische Diffusion zur Parametrisierung der physikalischen Diffusion verwendet. Dieser *kumulativen Habilitationsschrift* sind 16 Publikationen angehängt (eine kurze Beschreibung der wichtigsten Resultate f ndet man in Kapitel 1 und 3), deren Ziel es war, das Verständnis der Transportprozesse in der Stratosphäre und der oberen Troposphäre zu verbessern.

Contents

1 Introduction **1**
- 1.1 Composition of air in the UTLS region and its climatological relevance 1
- 1.2 Scientif c achievements presented in this “kumulative Habilitationsschrift” 2
- 1.3 Modeling of transport with CLaMS 6

2 Lagrangian transport with CLaMS **9**
- 2.1 Transport equations 9
- 2.2 Lagrangian view of transport 12
- 2.3 Aspect ratio and vertical diffusivity 15
- 2.4 Numerical diffusion 17
- 2.5 Entropy- and static stability-based grid 19
- 2.6 Re-gridding procedure 24
- 2.7 Closing remarks 27

3 Scientif c achievements: Composition of air in the UTLS region **29**
- 3.1 Asian summer monsoon and the seasonality of tropical ozone 29
- 3.2 Mixing-driven origin of the ExTL and TIL 33
- 3.3 Climatological relevance of mixing and interpretation of trends 38

4 Relevant publications **43**

A Appendix **49**
- A.1 Vertical velocity 49
- A.2 Effective horizontal diffusivity 51
- A.3 Interpolation and numerical diffusion 53
- A.4 Idealized 2D f ows 54
- A.5 Lyapunov exponents 55
- A.6 Next neighbors, Delaunay triangulation and Voronoi polygons 57

Bibliography **61**

1 Introduction

1.1 Composition of air in the UTLS region and its climatological relevance

Stratosphere-troposphere exchange (STE) across the tropopause is an important bi-directional process inf uencing the composition of the upper troposphere and lower stratosphere (UTLS, *Holton et al.* (1995)) and, consequently, the Earth's radiative budget (*Solomon et al.*, 2010; *Riese et al.*, 2012). The composition of air entering the stratosphere is mainly determined by the transport processes within the tropical tropopause layer (TTL) coupling the Hadley circulation in the tropical troposphere (time scale of days) with the much slower (time scale of months) Brewer-Dobson circulation in the stratosphere (*Fueglistaler et al.*, 2009). Complementary to the upward transport through the TTL, the downwelling branch of the Brewer-Dobson circulation is associated with the stratosphere-to-troposphere exchange that mainly occurs in the extratropics within the Extratropical Upper Troposphere Lower Stratosphere (ExUTLS) (*Gettelman et al.*, 2011) (see f g. 1.1).

The Brewer-Dobson circulation is overlaid by a fast (timescale of days to weeks), quasi-horizontal transport associated with isentropic mixing, i.e. two-way irreversible transport, including STE (*Holton et al.*, 1995). Note that this bi-directional isentropic mixing does not inf uence the distribution of mass (because these two mass f uxes are almost equal), but signif cantly affects the distribution of chemical species due to the dependence of tracer transport on the horizontal gradients of the considered species. Furthermore, transport of tropospheric air into the

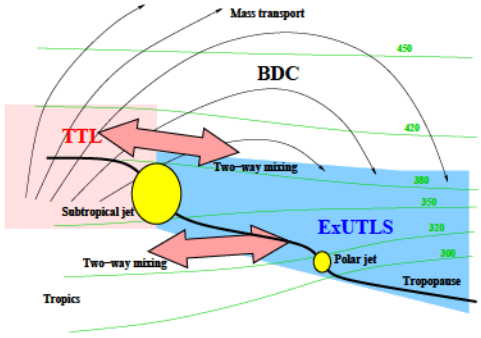

Figure 1.1: A schematic structure of the upper troposphere lower stratosphere (UTLS) region overlaid with the Brewer-Dobson circulation (BDC). TTL - Tropical Tropopause Layer, ExUTLS - Extratropical Upper Troposphere Lower Stratosphere. For a more detailed discussion of these atmospheric compartments see *Holton et al.* (1995), *Fueglistaler et al.* (2009) and *Gettelman et al.* (2011).

stratosphere is not zonally symmetric. Regionally (i.e. zonally) resolved studies suggest that the youngest air can be found in winter above the West Pacif c warm pool (seasons are related to the northern hemisphere (NH)) whereas in summer the Asian summer monsoon anticyclone forms the key pathway for transport into the stratosphere (*Fueglistaler et al.*, 2004; *Randel et al.*, 2010).

A better understanding of transport across the tropical tropopause layer (TTL) which acts as a "gateway to the stratosphere" plays a key role in understanding of the variability of the stratospheric concentrations of water vapor and other chemical species (*Fueglistaler et al.*, 2009). As f rst suggested by *Brewer* (1949), freeze-drying at the tropical tropopause causes strong dehydration from large tropospheric to very low stratospheric mixing ratios (e.g. *Randel and Jensen*, 2013). The variability of stratospheric water vapor has received considerable attention because of its key impact on the radiation budget and hence on surface climate (*Solomon et al.*, 2010; *Dessler et al.*, 2013).

Because of very low temperatures in this region, the UTLS has a key inf uence on radiation escaping the troposphere into space and hence affects surface climate and climate feedbacks (*Gettelman et al.*, 2011; *Riese et al.*, 2012) (see f g. 1.2). *Stevenson et al.* (2006) point to large model differences in the representation of STE, which result in considerable uncertainties in the simulated ozone budget, in particular in the upper troposphere. *Solomon et al.* (2010) highlight the fact that global models are rather limited in their representation of key processes determining the distribution and variability of lower stratospheric water vapor. *Riese et al.* (2012) assess the inf uence of uncertainties in the atmospheric mixing strength on global UTLS distributions of greenhouse gases (water vapor, ozone, methane, and nitrous oxide) and associated radiative effects. The results of such sensitivity studies show that the radiative effects of water vapor and ozone, both characterized by steep gradients in the UTLS, are particularly sensitive to the uncertainties in our knowledge of the atmospheric mixing strength. Globally averaged uncertainties of radiative forcing are about 0.72 and 0.17 W/m^2 for water vapor and ozone, respectively. Note that these values are comparable with the radiative forcing due to the anthropogenic effect of CO_2 ($\approx$ 1.6 W/m^2, *IPCC, 2013*).

1.2 Scientif c achievements presented in this "kumulative Habilitationsschrift"

This Habilitationsschrift is based on 16 papers which were published during and after 2009 and are appended to the text. All these contributions are related to different process-oriented and climate-relevant topics in the UTLS. An important scientif c tool used in almost all publications which are relevant for this "kumulative Habilitationsschrift" is the Chemical Lagrangian Model of the Stratosphere (CLaMS). CLaMS is a Chemistry Transport Model that has been developed and operated by Forschungszentrum Jülich at IEK-7. The Lagrangian transport part of the model, including the choice of the coordinates, the Lagrangian grid, diabatic trajectory calculations and

mixing are my own contributions (*McKenna et al.*, 2002; *Konopka et al.*, 2004, 2007; *Ploeger et al.*, 2010; *Konopka et al.*, 2010; *Ploeger et al.*, 2011; *Konopka et al.*, 2012).

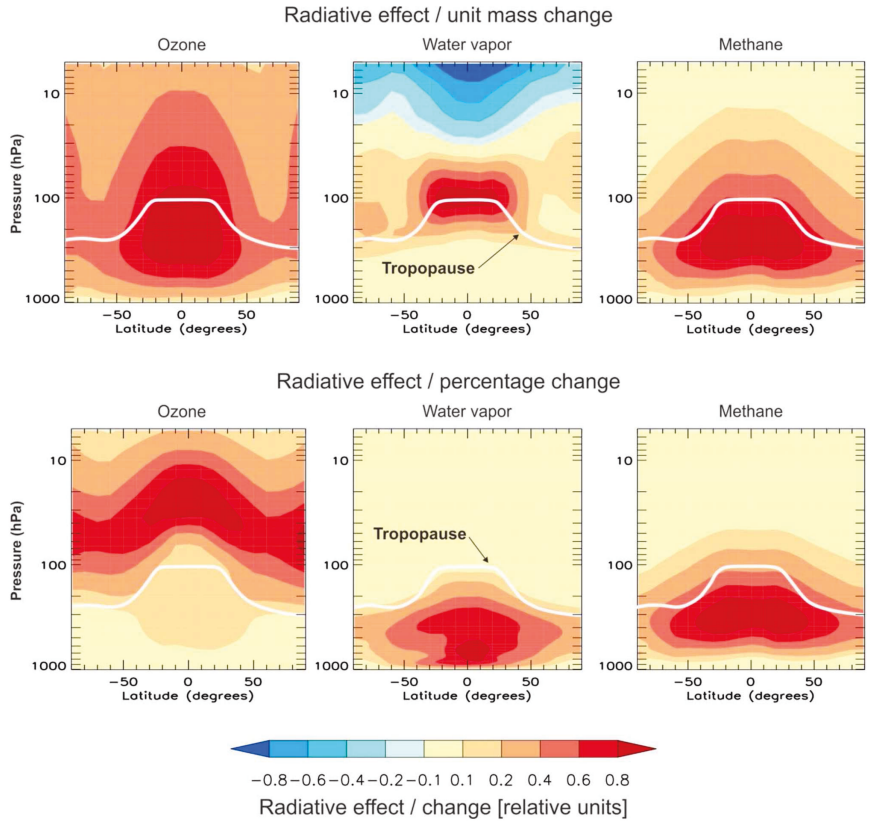

Figure 1.2: Sensitivity of surface temperature to the altitude and latitude of (left) ozone, (middle) water vapor, and (right) methane changes. Shading shows relative impact on surface temperature, measured as radiative effect, from either (top) unit mass increases or (bottom) percentage increases applied at individual latitudes and altitudes (1 km thick layers). For each trace gas, the calculated radiative effects have been normalized to the respective maximum value. Red colors indicate warming and blue colors cooling. The f gure shows, for example, that the impact on surface temperature of an ozone unit mass change at 100 hPa at the equator is about a factor of 2 larger than the impact of the same change at 10 hPa (adapted from *Riese et al.* (2012)).

Felix Ploeger wrote both papers during his PhD work that was supervised by Prof. Martin Riese and myself. The related scientif c questions, especially in the context of my personal contributions, can be divided into the following three f elds:

1. **Asian summer monsoon and the seasonality of tropical ozone in the lower stratosphere**

   Near-equatorial ozone observations from balloon and satellite measurements reveal a large annual cycle in ozone in the TTL above the tropical tropopause. The relative amplitude of the annual cycle is large in a narrow vertical layer between 16 and 19 km, with a change of approximately a factor of 2 in ozone between the minimum (during NH winter) and maximum (during NH summer, see *Randel et al.* (2007a) and references therein). The classical explanation of this pronounced annual cycle assumes that it is only due to the seasonality of the vertical velocities in the TTL (upwelling) and of ozone production. In this picture, the TTL is well-isolated with respect to the meridional transport, so that only vertical transport, which is faster in winter than in summer, is responsible for this large annual cycle (*Folkins et al.*, 2006; *Schoeberl et al.*, 2006; *Randel et al.*, 2007a).

   Here, the most important result of my research, mainly based on two first author publications *Konopka et al.* (2009) and *Konopka et al.* (2010), is that there is a strong seasonal cycle of meridional transport from the extratropics into the tropics, termed in-mixing, determining the composition of air in this region. Here, the Asian summer monsoon anticyclone plays a crucial role driving strong exchange between the tropics and high latitudes. Different aspects of this view are extended in two follow-up papers: *Ploeger et al.* (2012) and *Abalos et al.* (2013). The idea for the first study arose from discussions with Felix Ploeger on how to quantify in-mixing from all available observations. The results published by *Abalos et al.* (2013) reconcile the differences in quantifying in-mixing, which were found between the Eulerian and the Lagrangian-based diagnostics.

   Our interpretation of the tropical ozone seasonality also manifests in the respective seasonality of the mean age of air as recently discussed in *Konopka et al.* (2015). By analyzing the zonally averaged continuity equation for age of air, we decompose the seasonality of age of air into the contributions of residual circulation and eddy mixing. Thus, in the tropical lower stratosphere between $\pm 30^{\circ}$, the air becomes younger during boreal winter and older during boreal summer. During boreal winter, the decrease of age of air due to tropical upwelling outweighs aging by isentropic mixing. In contrast, weaker isentropic mixing outweighs an even weaker upwelling in boreal summer and fall making the air older during these seasons. Thus, older air and higher ozone in the summer TTL above the tropical tropopause are two sides of the same coin known as in-mixing, i.e. of enhanced meridinal transport from the mainly NH extratropics into the TTL and mainly driven by the Asian summer monsoon anticyclone.

2. **Mixing-driven origin of the Extratropical Transition Layer (ExTL) and of the Tropopause Inversion Layer (TIL)**

   Frequent mixing of stratospheric and tropospheric air in the vicinity of the tropopause forms a transition or mixing layer, termed the Extratropical Transition Layer (ExTL) which can be understood as a subset of the ExUTLS (*WMO*, 2003; *Gettelman et al.*, 2011). The highest val-

ues of the Brunt-Vaisala frequency N^2 are located above the tropopause within the tropopause inversion layer (TIL), where the vertical temperature gradient exhibits a pronounced inversion (*Birner et al.*, 2002; *Birner*, 2006). While the TIL is def ned by the exceptional dynamical property of the atmosphere (high static stability), the def nition of the ExTL is mainly based on a unique composition containing both tropospheric *and* stratospheric signatures (mixing layer).

Using mixing parametrization in CLaMS as well as *in situ* observations it was possible to show that the ExTL is well-represented in the model (*Vogel et al.*, 2011) and that this layer itself is mainly formed by (isentropic) eddy mixing on synoptic to seasonal time scales (*Pan et al.*, 2009; *Konopka and Pan*, 2012). All these three papers are the result of a collaboration between IEK-7, Forschungszentrum Jülich, and the Atmospheric Chemistry Division in NCAR (Boulder, USA), especially with Dr. Laura Pan and Dr. William Randel. Dr. Bärbel Vogel and myself participated in the Stratosphere-Troposphere Analyses of Regional Transport (START08) campaign to study the chemical and transport characteristics of the ExTL using the NSF/NCAR HIAPER aircraft.

There is still an ongoing debate on the physical mechanisms leading to the formation of the TIL. One of these mechanisms, based on radiative cooling of a well-mixed ExTL, was f rst proposed by *Randel et al.* (2007b) and discussed by *Kunz et al.* (2009). This paper is part of Anne Kunz’s PhD work supervised by Dr. Cornelius Schiller and myself. Our analysis shows that the TIL is a part of the ExTL, i.e. of a well-mixed transition layer containing both tropospheric and stratospheric signatures, in particular relatively high mixing ratios of water vapor (*Kunz et al.*, 2009). Following *Kunz et al.* (2009), the TIL consists of air parcels with “old” or “frozen-in” mixing, which took place on a seasonal rather than a synoptic time scale.

3. **Climatological relevance of mixing and interpretation of trends**

CLaMS is a Chemistry Transport Model driven by prescribed meteorology (mainly by the ERA-Interim reanalysis), which can also be applied for understanding trends in atmospheric composition and transport. *Riese et al.* (2012) investigates the inf uence of uncertainties in the atmospheric mixing strength on global distributions of greenhouse gases (water vapor, ozone, methane, and nitrous oxide) and discuss the associated radiative effects. My contribution to this work was to provide the CLaMS model for this type of sensitivity study (i.e. with respect to mixing).

Wang et al. (2012) analysed the tropospheric ozone trends by comparing the long term observations over Beijing (2002-10) with the CLaMS model. Following *Wang et al.* (2012), a clear positive trend for the column ozone in the lower troposphere (0-3 km) during spring and summer can be deduced from the observations. Using CLaMS, *Wang et al.* (2012) have also shown that this trend does not result from the trend of transport of stratospheric ozone down to the boundary layer but much more from the pollution-driven O_3 formation, mainly as a

consequence of increased industrial and traffic activities in and around Beijing. This publication, which was supervised by myself, was a part of Yong Wang's PhD work (submitted by the University of Beijing, co-supervised by Prof. Yi Liu).

The stratospheric water vapor entry values derived from almost three decades of satellite observations roughly follow the evolution of tropical tropopause temperatures and show multi-timescale variations ranging from daily to decadal (*Fueglistaler and Haynes*, 2005; *Fueglistaler et al.*, 2013; *Urban et al.*, 2014; *Hegglin et al.*, 2014). In a case study of a remarkable major Sudden Stratospheric Warming (SSW) during boreal winter 2008/09, *Tao et al.* (2015a) investigate how transport and mixing triggered by this event affect the composition of the entire stratosphere in the northern hemisphere. There is ongoing PhD work by Mengchu Tao in Forschungszentrum Jülich at IEK-7 (within the Helmholtz Graduate School HITEC) that is supervised by myself and co-supervised by Prof. Michael Volk at the University of Wuppertal).

Following *Tao et al.* (2015a), we found that the major SSW event, at the same time, accelerates polar descent and tropical ascent of the Brewer-Dobson circulation. The accelerated ascent in the tropics and descent at high latitudes first occurs in the upper stratosphere and then propagates downward to the lower stratosphere. This downward propagation in the tropics takes over one month and influences the water vapor budget at the tropical tropopause.

In a second recently published paper *Tao et al.* (2015b) systematicaly investigate all major SSWs in the last 35 years, especially with respect to their impact on the amount of water vapor entering the stratosphere during boreal winter. Our results show that this effect is strongly modulated by the phase of the quasi-biennial oscillation (QBO). We suggest that the enhanced dehydration due to the major SSWs combined with a higher frequency of major SSWs after the year 2000 may have contributed to the lower stratospheric water vapor observed after 2000.

1.3 Modeling of transport with CLaMS

CLaMS is a Lagrangian Chemistry Transport Models (CTM) suitable for simulating atmospheric transport and chemistry from the boundary layer all the way to the top of the stratosphere (50 km altitude). CLaMS integrates a hierarchy of models ranging from a simple box model to a 3D CTM driven by meteorological winds available from meteorological services such as European Centre for Medium-Range Weather Forecasts (ECMWF), United Kingdom Met Office (UKMO) and National Center for Environmental Prediction (NCEP). CLaMS contains separate modules for transport, mixing, chemistry, and microphysics that can be included or excluded (see *Pommrich et al.* (2014) and references therein).

Compared with other CTMs, the novel approach of CLaMS is its description of atmospheric mixing, especially in the stratosphere where vertical mixing is extremely weak due to a strong

vertical stability. Whereas the common approach is to minimize the numerical diffusion ever present in the modeling of transport, CLaMS is a first attempt to apply this "undesirable disturbing effect" to parameterize the "true" physical mixing. By using some scaling properties of numerical diffusion which are the same as of the atmospheric diffusivity (see sections 2.3 to 2.5), and by applying numerical regridding only to those parts of the grid where physical mixing is expected anyway due to strong deformation rates of the Lagrangian air parcels (see section 2.6), this novel parameterization of mixing was included into the well-known pure Lagrangian, i.e., trajectory-based transport.

Due to a high vertical stability in the stratosphere, the vertical transport is suppressed and the resulting, almost 2d horizontal (isentropic) flow is usually described as chaotic advection. This 2d turbulence manifests in formation of strong horizontal gradients of trace gases distributions, mainly in the vicinity of jets acting as isentropic transport barriers. The challenge for modeling of transport is to resolve strong spatial and temporal variability of such tracer distributions, mainly in view of undergoing no-linear chemistry like chlorine-induced ozone loss processes within the polar vortex. CLaMS was the first Lagrangian Chemistry Transport Model where all these processes were successfully implemented and validated by comparison with in-situ and satellite data. In the next chapter, the main concepts of atmospheric transport in CLaMS, especially the implementation of mixing will be included step-by-step.

2 Lagrangian transport with CLaMS

In the following we discuss the question why the Lagrangian view of transport offers advantages if compared to the more common Eulerian view and how these advantages are implemented in CLaMS (for the sake of convenience chemistry will be excluded in this chapter). In particular section 2.1 repeats the well-known equations of transport, section 2.2 re-formulates these equation in the Lagrangian frame of reference and section 2.3 discusses how these equations describe the real atmosphere through a right choice of the vertical and horizontal scales and respective diffusivities. The novel aspects of CLaMS are formulted in sections 2.4 to 2.6 where the numerical diffusion due to regridding within the (irregular) Lagrangian grid is related to physical mixing.

2.1 Transport equations

The atmosphere extending between the Earth's surface and the mesosphere can usually be understood as a thermodynamic f uid with m species. Most of these species undergo different types of chemical reactions and interact via radiation with both the Sun and the Earth. These species also interact via boundary conditions with the Earth's surface and with the upper atmosphere beyond the mesosphere where the extremely low density of the air restricts the applicability of thermodynamics. The momentum, energy and m continuity equations describe such a system. Some further assumptions, which are widely used in the atmospheric dynamics reduce these general balances to the so-called primitive equations (see e.g. *Holton*, 1992; *Vallis*, 2006). Within the climate modeling community, this set of primitive equations is also denoted as dynamical core (*Satoh*, 2014).

Roughly speaking, the dynamical core def nes the governing equations on resolved scales, while the parametrizations represent unresolved subgrid scale processes like gravity waves or microphysics (*Thuburn*, 2008). Generally, due to its complexity, the dynamical core can only be solved numerically. Equations of transport, also denoted as continuity or mass balance equations, in particular those for trace gases or aerosols, can make up a dominant part of the dynamical core at least in terms of the total computational cost if the number of the considered species m becomes large (*Lauritzen et al.*, 2011).

By using the Reynolds averaging procedure, we formulate now these equations in the local (i.e. differential) formulation. Let us consider an air parcel containing m chemically passive species (tracers) with number densities n_i (in $1/m^3$), molecular masses M_i (in kg), mass densities

$\rho_i = M_i n_i$ (in kg/m^3) and volume mixing ratios μ_i (dimensionsless) given as

$$n_i = n\mu_i, \quad i = 0, ..., m, \tag{2.1}$$

where $n = n_0$ ($\mu_0 = 1$) denotes the total number density of all molecules. Similarly, $\rho = \rho_0 = Mn$ denotes the mass density of air with the mean molecular mass of air given by $M = M_0$

Thus, the (local) continuity equations for a suff ciently small but still macroscopic scale (i.e. containing a suff ciently large number of molecules justifying such thermodynamic quantities as temperature or entropy) is given as

$$\partial_t n_i + \nabla \cdot (n_i \mathbf{u}) = 0, \qquad i = 0, ..., m, \tag{2.2}$$

where $\mathbf{u} = (u, v, w)$ denotes the f ow velocity, and molecular diffusion processes are neglected.

Assuming (Reynolds averaging procedure, see e.g. *Batchelor* (1953)):

$$\mathbf{u} = \bar{\mathbf{u}} + \mathbf{u}' \qquad n_i = \bar{n}_i + n_i', \tag{2.3}$$

with $\bar{\mathbf{u}}$, $\bar{n}_i$ denoting mean winds and mean number concentations on horizontal scales of about 10-100 km (e.g. from meteorological data) and with $\mathbf{u}'$, n_i' describing respective f uctuations (i.e. unresolved sub-grid processes such as gravity waves). Then, with $\overline{\mathbf{u}'} = \overline{n_i'} = 0$, the mean f ux density $\bar{\mathbf{j}}_i$ is given as

$$\bar{\mathbf{j}}_i = \overline{n_i \mathbf{u}} = \bar{n}_i \bar{\mathbf{u}} + \overline{\mathbf{u}' n_i'} = \bar{n}_i \bar{\mathbf{u}} + \mathbf{j}_i'. \tag{2.4}$$

Here, $\bar{n}_i \bar{\mathbf{u}}$ and $\mathbf{j}_i'$ abbreviate mean advective f ux and an additional, unresolved mass transport, in the following referred to as mixing. Note that mixing, although mainly characterized as a diffusive (turbulent) part of the f ow, can also consist of unresolved advective contributions (e.g. stirring in a non-linear f ow). Commonly, mixing is parametrized by Fick's law (*Fick*, 1855) and by the additional assumption that only the gradient of the mixing ratios $\bar{\mu}_i$ is relevant for mixing (*Hall and Plumb*, 1994), i.e.:

$$\mathbf{j}_i' = \mathbf{D} \cdot \nabla \bar{n}_i = \bar{n} \mathbf{D} \cdot \nabla \bar{\mu}_i \tag{2.5}$$

with the diffusion tensor $\mathbf{D}$ that, following Onsager's symmetry theorem, is given as a 3×3 symmetric matrix (*Onsager*, 1931).

In the real atmosphere, the vertical and horizontal diffusive f uxes are very different, so $\mathbf{D}$ reduces to two horizontal and vertical diffusivities D_h and D_v by assuming that the atmosphere is invariant to horizontal rotations and by neglecting the still remaining two off-diagonal elements D_{xy} (*Lyubarski*, 1960), i.e.

$$\mathbf{D} = \begin{pmatrix} D_h & D_{xy} & 0 \\ D_{xy} & D_h & 0 \\ 0 & 0 & D_v \end{pmatrix} \approx \begin{pmatrix} D_h & 0 & 0 \\ 0 & D_h & 0 \\ 0 & 0 & D_v \end{pmatrix}. \tag{2.6}$$

Note that the def nition of the diffusivities strongly depends on the def nition of the resolved and unresolved spatial scales which, in practice, cannot be exactly f xed.

Consequently, transport of species is governed by the following equations (we simplif ed the notation and omitted the bars):

$$(\partial_t + \mathscr{L})\, n_i = 0, \quad \mathscr{L}(n_i) := \nabla \cdot [(\mathbf{u} + \mathbf{D} \cdot \nabla)\, n_i] \tag{2.7}$$

with the operator $\mathscr{L}$ consisting of the advective (**u**) and diffusive (**D**) part of transport, or, with $n_i = n\mu_i$,

$$\partial_t (n\mu_i) + \nabla \cdot (n\mu_i \mathbf{u} + n\mathbf{D} \cdot \nabla \mu_i) = 0, \quad i = 0, ..., m. \tag{2.8}$$

In particular, the transport of all air molecules n reduces with $i = 0$ and $\mu_0 = 1$ ($\Rightarrow \nabla\mu_0 = 0$) to

$$\partial_t n + \nabla \cdot (n\mathbf{u}) = 0 \tag{2.9}$$

describing the conservation of the total number density n or of mass density $\rho = Mn$ (M - mean molecular mass of air). Note that transport of mass is driven only by the f ow velocity **u** whereas, in addition to this advective f ux, the species-dependent diffusive f uxes determine the distributions n_i (or mixing ratios μ_i) of each chemical species i.

The last two equations can also be rewritten as:

$$n \frac{D}{Dt} \mu_i + \nabla \cdot (n\mathbf{D} \cdot \nabla \mu_i) = 0, \quad i = 1, ..., m \tag{2.10}$$

and

$$\frac{D}{Dt} \rho + \rho \nabla \cdot \mathbf{u} = 0\,, \tag{2.11}$$

with the material derivative

$$\frac{D}{Dt} := \partial_t + \mathbf{u} \cdot \nabla\,, \quad \nabla = (\partial_x, \partial_y, \partial_z), \quad \mathbf{u} = (u, v, w) \tag{2.12}$$

In f uid mechanics incompressible f ow (isochoric f ow) refers to a f ow in which the material density is constant within the air parcel, i.e. $D\rho/Dt = 0$. Thus, for incompressible f ows (although with a f nite speed of sound), eq. (2.11) reduces to

$$\nabla \cdot \mathbf{u} = 0\,. \tag{2.13}$$

Reversely, in a divergence- *and* mixing-free f ow, the transport equations reduce to

$$\frac{D\rho}{Dt} = 0, \qquad \frac{D\mu_i}{Dt} = 0, \quad i = 1, \ldots, m \tag{2.14}$$

sometimes denoted as a pure advection problem (*Lauritzen et al.*, 2011).

Because the spatial and temporal distribution of the atmospheric trace gases determines the chemical and, consequently, also radiative properties of the atmosphere, the quality of the solutions of transport equations has a strong inf uence on the whole atmospheric system. For example, an appropriate description of transport barriers like the edge of the polar vortex (*Tuck*, 1986),

the tropical pipe (*Plumb*, 1996) or the extratropical tropopause (*Holton et al.*, 1995) is prerequisite for a quantitative understanding of the Brewer-Dobson circulation or of the chlorine- and bromine-induced ozone loss in the polar stratosphere.

Thus, on the one hand, trace gas distributions derived from transport equations significantly influence atmospheric dynamics (e.g. via chemistry and radiation). On the other hand, (only) these distributions can be compared with observations (which can hardly be done for dynamical quantities like vertical velocity or vorticity) and, in this way, provide a basis for the validation of the models.

Numerical formulation of the atmospheric transport discretizes the governing physical equations, both in time and space, by using some appropriate values of the time step Δt and of the horizontal/vertical resolution $\Delta x/\Delta z$, respectively (see fig. 2.1). For reasons of simplicity, in the following conceptual discussion we reduce the horizontal space to only one coordinate x. If the 2D (horizontal) distance between 2 points is considered we use the notation $r = \Delta r$.

Generally, the following two requirements are crucial. First, because the horizontal and vertical scales of atmospheric variability are very different, an appropriate choice of the respective spatial resolution is necessary. Within a numerical model this means that both scales have to be resolved with the "same quality" everywhere within the considered atmospheric domain (*Lindzen and Fox-Rabinovitz*, 1989). Second, the numerical errors of the solution of the governing differential equations should be minimized. In particular, the numerical noise has to be smaller than the modeled physical quantities. A prominent example of such errors is the numerical diffusion that depends on both spatial and temporal resolution and is expected to be smaller than the physical diffusivity (*Rood*, 1987; *Schoeberl and Douglass*, 2010; *Lin et al.*, 2013).

2.2 Lagrangian view of transport

The focus of this section is to work out the advantages of the Lagrangian view of transport over the commonly used Eulerian description. Thus, the Eulerian frame of reference is a way of looking at fluid motion from a perspective that is fixed in space. In contrast, in the Lagrangian approach, the observer follows individual fluid parcels as they move (see fig. 2.1). Using a grid model means that the Eulerian grid is fixed in space while the Lagrangian grid moves, materially anchored, with the flow.

In the following, we use the term air parcel for the pivotal points of such a grid. Thus, air parcels are massless and either fixed in space (Euler) or in the fluid (Lagrange). From the perspective of eq. (2.10), the only difference between the Eulerian and Lagrangian frames of reference arises from the fact that in the Lagrangian system $\mathbf{u} = 0$ can be assumed and, consequently, eq. (2.10) describes diffusive transport relative to the center of the air parcel, i.e.

$$n\frac{d}{dt}\mu_i + \nabla \cdot (n\mathbf{D} \cdot \nabla \mu_i) = 0, \quad i = 1, ..., m \tag{2.15}$$

whereas the path of each air parcel, $\mathbf{r}(t)$, is the solution of the trajectory equation, i.e.

$$\frac{d\mathbf{r}(t)}{dt} = \mathbf{u}(\mathbf{r}(t),t), \quad \mathbf{r}(0) = \mathbf{r}_0. \tag{2.16}$$

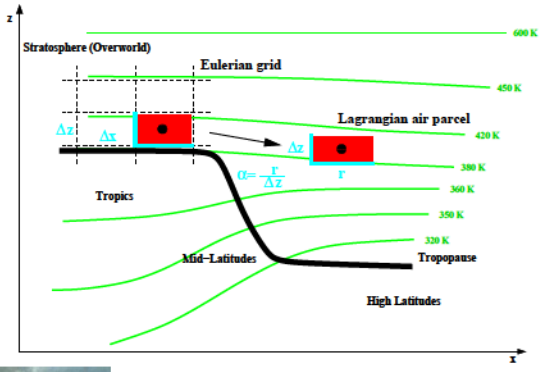

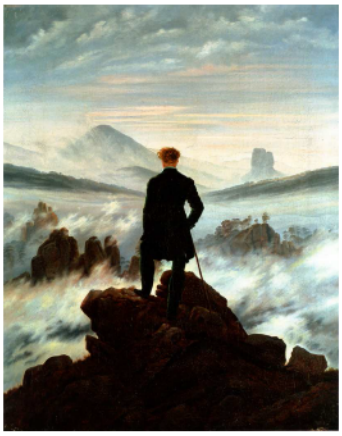

Figure 2.1: Top: Eulerian grid fixed in space versus Lagrangian grid moving with the flow. The bold black points denote the air parcels which can be understood as massless, pivotal points fixed either in space (Euler) or in the fluid (Lagrange). In both frames of reference, the horizontal and vertical resolutions Δx (or $r = \Delta r$ describing the 2D horizontal distance between the air parcels) and Δz should be consistently chosen. Bottom: ...and a slightly more artistic view: Left: Casper David Friedrich's famous "Wanderer above the Sea of Fog", who looks at the atmosphere passing him by (Eulerian view). Right: Montgolfier balloon over Rocamadour moves approximately with the atmosphere (Lagrangian view).

Thus, according to eq. (2.15), the time dependence of μ_i is determined only by mixing. $\mathbf{D} = 0$, i.e. no mixing, implies that the mixing ratios μ_i are constant.

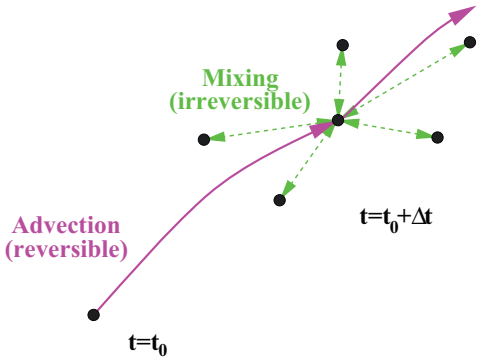

Figure 2.2: Lagrangian transport can be understood as a consecutive sequence of advection (trajectories driven by the wind) and mixing (mass exchange between adjacent air parcels). Whereas advection is reversible (i.e. backward trajectory driven by the reversed velocity field exactly reproduces the starting point), mixing defines the irreversible part of transport (i.e. after mixing the original mixing ratios of the air parcel cannot be reproduced).

If the (irregular) Lagrangian air parcels are tracked throughout the simulation, the resulting scheme is referred to as fully Lagrangian. However, the Lagrangian air parcels may be remapped after every time step Δt on a regular Eulerian (background) grid. Such an approach is referred to as semi-Lagrangian (*Lauritzen et al.*, 2011). In both frames of reference, the physical properties at a given grid point describe the mean properties of the atmosphere within the volume of the grid box surrounding this point.

Generally, atmospheric mixing is an irreversible process that mixes chemical species on the molecular scale. However, most of the relevant processes are governed by much coarser scales. On such scales, mixing is driven by the macroscopic turbulence, known as eddy diffusion, with eddy diffusivity being several orders of magnitude larger than molecular diffusivity.

Mixing in fluid dynamics is, irrespective of the resolved scales, the irreversible part of transport. In contrast, advection, the reversible part of transport, is controlled by the 3D velocity field (fig. 2.2). This partitioning into the reversible and irreversible parts, i.e. into advection and mixing, can be clearly carried out using the Lagrangian perspective. From this perspective, trajectories, which are related to the wind fields, describe the advection of the air parcels. The transfer of mixing ratios between such air parcels, independent of its specific realization, defines mixing (for a more formal definition of irreversibility see *Schröter* (1995)).

Usually, the Eulerian approach is based on a grid with the horizontal and vertical mesh widths Δx, Δz. The Lagrangian approach, on the contrary, is based on an irregular grid of air parcels with the mean horizontal and vertical separations r, Δz. In the following, the geometric altitude z or the dry potential temperature θ is used as the vertical coordinate (*Kasahara*, 1974). Alternatively, a hybrid coordinate ζ will be used (*Mahowald et al.*, 2002) to resolve both transport processes in the troposphere influenced by the orography and transport processes in the stratosphere where adiabatic horizontal transport dominates. The corresponding vertical velocity $\dot{\theta}$ (or $\dot{\zeta}$) is referred to as diabatic vertical velocity (appendix A.1)

In summary, Lagrangian transport means that an irregular grid of air parcels, materially anchored with the flow, describes the temporal evolution of the flow composition. As time pro-

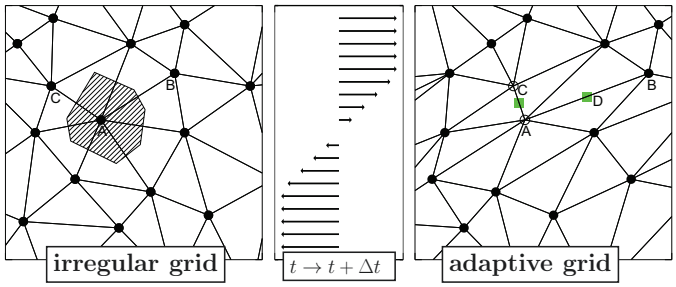

Figure 2.3: Adaptive grid procedure (adapted from *McKenna et al.* (2002)). A 2D, irregular grid of air parcels undergoes deformation in a shear f ow. The Delaunay triangulation (appendix A.6) determines the next neighbors (C and B are neighbors of A) and the volume of A can be def ned by the Voronoi polygon (dashed area, see also appendix A.6). After a time step Δt the re-gridding procedure is applied to the deformed grid. Interpolations of the transported species on the new air parcels (green) cause numerical diffusion which, within a Lagrangian transport scheme, can be used to parameterize mixing between the air parcels.

gresses, the adaptation or re-gridding procedures may be necessary to avoid some clustering of the air parcels, i.e. to restore the uniform distribution of the grid points. Such procedures result in some (undesirable) numerical diffusion due to the associated interpolations.

One of the most intriguing features offered by Lagrangian transport is the possibility to apply such numerical diffusion to parameterize the "true" physical mixing. For the f rst time this concept was successfully implemented in CLaMS (*McKenna et al.*, 2002; *Konopka et al.*, 2004, 2007) and is based on the the dynamically adaptive, or simply adaptive Lagrangian grid procedure (f g. 2.3, adaptive means here self-adjusting during the integration time).

2.3 Aspect ratio and vertical diffusivity

Let us come back to our Lagrangian formulation of transport, i.e. to eqs. (2.15) and (2.16). To get a physical interpretation of these equations and their solution we have to answer the following questions: which typical horizontal and vertical scales in the real atmosphere are represented by the Lagrangian air parcels and what are the typical spatial scales on which D_h and D_v parametrize atmospheric mixing?

Generally, the vertical variability of the atmosphere is much stronger compared with that along the same horizontal scale where gradients of the atmospheric properties are much weaker. Thus, the aspect ratio $\alpha = \Delta x / \Delta z$ def ning the ratio between the scales of the horizontal and vertical variability Δx and Δz is typically a large number of the order of ≈ 100. High values of α dominate the stably stratif ed parts of the atmosphere, whereas in regions with strong convection α

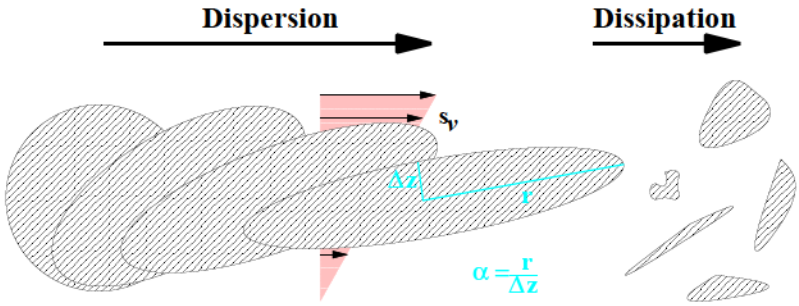

Figure 2.4: Dispersion versus dissipation. Elongation or dispersion of a spherical Gaussian plume in a sheared f ow with a shear rate s_v. When the aspect ratio $\alpha = r/\Delta z$ exceeds a critical number, typically larger than 100, the plume dissipates, i.e. mixing sets in and the plume becomes indistinguishable from the background atmosphere.

decreases. The quantitative values of α are controlled by the turbulent diffusion that is strong in the troposphere and rather weak and patchy in the stratosphere. The turbulence itself is driven by the energy cascade from large almost 2D horizontal eddies which are formed by breaking waves on a planetary scale and which decay into smaller and smaller 3D eddies.

A simple example (see f g. 2.4) of how large values of α arise in the atmosphere is obvious from the dispersion of a spherical Gaussian plume (i.e. of a plume with a Gaussian tracer distribution) in a horizontal and linear shear f ow with a constant vertical shear s and constant vertical/horizontal diffusivities (*Konopka*, 1995; *Schumann et al.*, 1995; *Schlager et al.*, 1997) (for the def nition of a pure 2D shear and strain f ows see appendix A.4).

Thus, in a stably stratif ed and sheared f ow a spherical Gaussian plume becomes elongated. As shown in *Konopka* (1995), the aspect ratio α of such a plume increases with time t like $\approx (st)^2$, i.e. the original spherically symmetrical source is deformed into a strongly elongated and almost horizontal f lament that, in the real atmosphere, would dissipate after α exceeded a certain critical number. However, before dissipation occurs, i.e. before the Gaussian plume becomes indistinguishable from the background atmosphere, the values of α roughly quantify the asymmetry between the horizontal and vertical scales discussed here. Thus, a balance between dispersion and dissipation of the plume, or, in other words, between advection and mixing, def nes the atmospheric aspect ratio α.

Using a random-straining model describing a steady state of vertical diffusion, vertical shear and horizontal stirring, *Haynes and Anglade* (1997) argued that α estimates the ratio between the horizontal and vertical diffusivities D_h and D_v through

$$\alpha^2 = D_h/D_v. \tag{2.17}$$

Eq. (2.17) was derived on the assumption that the interaction of the vertical diffusion and of the vertical shear produces slanted f laments, which, after being transported by the (isentropic)

chaotic advection, form large-scale, horizontal, pancake-like structures which slowly dilute through stirring in a quasi-isentropic flow. *Haynes and Anglade* (1997) argued that in contrast to D_v, which is expected to be mostly independent on the vertical scales within the range $1 - 100$ m (mainly due to horizontal direction of the atmospheric winds), D_h has to be understood as an effective diffusivity, i.e. as a mean diffusive property that parametrizes transport occurring on unresolved scales and may contain some unresolved advective contributions.

D_h is expected to be of the order of 10^3 m^2/s (appendix A.2) Note that eq. (2.17) also implies that D_h is not an independent atmospheric parameter but can be derived from D_v and α. This fact underlines the importance of D_v which is expected to be in the range 10^{-4} to 1 m^2/s (*Woodman and Rastogi*, 1984; *Balluch and Haynes*, 1997; *Waugh et al.*, 1997), and if the method of diffusive reconstruction is applied, the stratospheric value of D_v varies between 0.01 inside the polar vortex, 0.1 in the surf zone and around 0.5 m^2/s in the subtropics (*Legras et al.*, 2005; *Pisso and Legras*, 2008; *James and Legras*, 2009). Using these values *Haynes and Anglade* (1997) estimated that α in the lower stratosphere is of the order of 250.

We conclude that the knowledge of the spatial variability scales, (i.e. of α and of either the horizontal or the vertical scale) and of D_v (D_h can be derived from (2.17)) can be understood as the minimum information about the atmosphere that allows us to solve the main transport equations discussed at the end of the last subsection. But, unfortunately, the situation becomes completely different if numerical errors disturb the solutions of these equations.

2.4 Numerical diffusion

The substantial difference between the Eulerian and Lagrangian approaches arises if eq. (2.2) has to be numerically solved. In the last 100 years many efforts have been made to find the "best" numerical treatment of eq. (2.2). As reviewed in (*Rood*, 1987; *Schoeberl and Douglass*, 2010), various Eulerian-based approaches have been applied where the time and spatial derivatives of the continuity equation are replaced by discrete, Taylor-series-based, approximations. *Courant et al.* (1928) formulated a criterion, known as the Courant-Friedrichs-Lewy (CFL) condition, stating that in order to achieve a stable numerical solution, the maximal time step of integration Δt is limited by the Eulerian grid size Δx and the maximal flow velocity u_c through $\Delta t < \Delta x / u_c$, i.e., all integrated quantities have to be re-interpolated on the background grid before the flow leaves the grid mesh (see fig. 2.5).

This is a strong limitation of the available time step Δt. For a typical, maximal wind velocity of the order of 100 m/s, a high frequency of the interpolations on the Eulerian background grid is required which manifests itself as an undesirable numerical diffusion. In particular, the horizontal numerical diffusion can be estimated as

$$D_h^{num} \approx \Delta x^2 / \Delta t \tag{2.18}$$

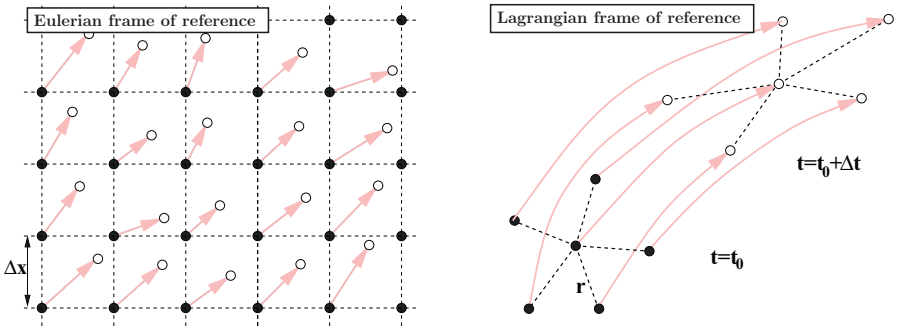

Figure 2.5: Numerical solution of eq. (2.10) requires the usage of a grid. This can be done within the Eulerian (left) or the Lagrangian (right) frame of reference

(appendix A.3) and for $\Delta x = 100$ km, $\Delta t = 10$ min (i.e. assuming $u_c = 100$ m/s) is of the order of 10^6 m^2/s, i.e. larger by three orders of magnitude than the (physical) effective horizontal diffusivity D_h which, following our previous discussion, is of the order of 10^3 m^2/s.

The semi-Lagrangian schemes developed in the last 15 years helped to reduce this problem by weakening the rigidity implied by the CFL condition, although to date only 2D formulations have been implemented (*Lin and Rood*, 1996; *Smolarkiewicz and Pudykiewicz*, 1992; *Lauritzen et al.*, 2011). *Lin and Rood* (1996) argued that the maximal spatial gradient of the wind velocity $\partial_x u \approx \Delta u/\Delta x$ (in 1/s) rather than the maximal wind velocity itself u_c determines the time step of integration Δt through the condition $\Delta t < (\partial_x u)^{-1} = \Delta x/\Delta u$. Thus, by assuming that typical values of Δu are smaller by a factor of 100 to 1000 than the values of u_c, the critical time step of integration becomes signif cantly larger than the corresponding Eulerian time step and, consequently, the numerical diffusion becomes comparable with the effective horizontal diffusivity discussed in the previous chapter.

Even from the full Lagrangian point of view, some interpolations or re-mapping procedures are necessary because the air parcels do not remain homogeneously distributed during the course of integration of the trajectory equation (2.16) mainly due to some inconsistencies in the wind f elds (*Stohl*, 1998). Thus, re-gridding procedures have to be used in order to sustain the spatial homogeneity of the air parcels and, consequently, some numerical diffusion is inevitable.

However, the full Lagrangian view offers an alternative to exploit the numerical diffusion for parametrization of the physical mixing rather than to f nd ways of avoiding this effect. This is supported by the fact that, using (2.18), the ratio between the horizontal and vertical numerical diffusion coeff cients can be estimated as

$$D_h^{num}/D_v^{num} \sim \Delta x^2/\Delta z^2 \approx r^2/\Delta z^2 = \alpha^2, \tag{2.19}$$

i.e. it mimics the “true atmosphere” as argued by *Haynes and Anglade* (1997) (see eq. (2.17)).

Thus, one possibility of parametrizing physical mixing between the neighboring air parcels is to use interpolations, e.g. as an appropriate re-gridding procedure.

In contrast to the Eulerian models where, due to the CFL condition, numerical diffusion is proportional to the flow velocity, i.e. $D_h^{num} \sim \Delta x^2/\Delta t = \Delta x\, u \sim u$, in Lagrangian models the relative rather than the absolute motion between the air parcels defines the necessity of grid readjustment. Following the same arguments as for the semi-Lagrangian schemes (*Lin and Rood*, 1996), the Lagrangian approach allows a realization with $D_h^{num} \sim \Delta x^2 \partial_x u$.

We conclude that in contrast to the Eulerian models where numerical diffusion is proportional to the flow velocity, i.e. $D_h^{num} \sim \mathbf{u}$ (*Courant et al.*, 1928), the Lagrangian approach allows a realization with $D_h^{num} \sim \nabla \mathbf{u}$. Thus, because it is expected that physical mixing is not driven by absolute velocity of the flow but rather by deformations induced by the shear and strain rates (*Smagorinsky*, 1963), the numerical diffusion of the Lagrangian transport schemes can be used to parameterize physical mixing.

In summary, from the Lagrangian point of view, two problems have to be solved. First, an appropriate (irregular) Lagrangian grid, defined through the parameters r and Δz, has to be found. Interpolations within such a grid can mimic physical mixing events only if the values of r and Δz are correctly chosen or, at least, if they scale properly with the vertical coordinate, i.e. by the transition from the well-mixed troposphere to the stably stratified stratosphere (we discuss this point in the next section). Second, a re-gridding mechanism has to be found to trigger such interpolations. More precisely, the re-gridding mechanism has to be controlled by some flow parameters which parametrize mixing in a physical way (more details in section 2.6).

2.5 Entropy- and static stability-based grid

A possible approach for defining the mean air parcel separations r and Δz is the requirement that each air parcel should contain the same number of air molecules or the same mass (e.g. *Reithmeier and Sausen*, 2000). If, in addition, a constant total number of air parcels can be assumed, mass conservation follows automatically – a condition hardly fulfilled by most transport schemes. An important disadvantage of such a distribution of air parcels is its scaling property due to the strong decrease of air density with altitude, with the consequence of too many air parcels in the lower troposphere and only very few in the mesosphere.

In the following, an alternative way of reasoning will be briefly outlined (for details see *Konopka et al.* (2012)) that is based on the idea that the spatial distribution of the entropy and the static stability may define a more physical spatial coverage of the whole atmosphere with air parcels. For the sake of convenience, we assume a dry atmosphere (how to generalize this concept to a moist atmosphere, see *Konopka et al.* (2012)).

Our first main assumption is to assign each air parcel the same amount of entropy s, related to

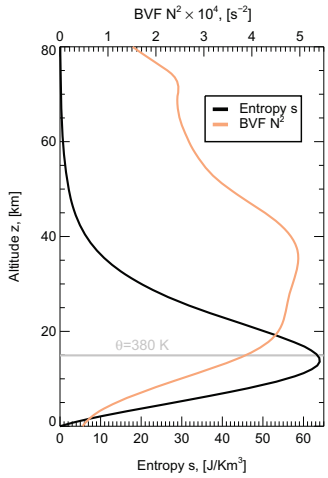

Figure 2.6: Entropy density s (black) and the Brunt-Vaisala frequency N^2 (orange) as derived from the US standard atmosphere.

the potential temperature θ through (*Holton et al.*, 1995):

$$s(\theta,\rho) = c_p \rho \ln \frac{\theta}{\theta_0} \tag{2.20}$$

with specif c heat c_p (J/(K kg), air mass density ρ (kg/m^3) and the reference potential temperature θ_0 being the temperature T_0 that the air parcel would acquire if adiabatically brought (i.e. with $s = \text{const}$) to a standard reference pressure p_0.

According to this def nition, s describes the entropy density, i.e. the amount of entropy per volume unit (J/(K m^3). Using prof les of the US standard atmosphere, s calculated from eq. (2.20) is plotted in f g. 2.6 (black) showing a clear maximum around 15 km. This is because θ increases while ρ decreases with altitude and, consequently, s, which is proportional to $\rho \ln \theta$, has a maximum.

In a system where no additional information is available, the same entropy per air parcel means that each air parcel contains the same amount of available energy that is transferable into work (strictly speaking, under the same thermal conditions). From a thermodynamic point of view, motion in the atmosphere is a result of work imposed by different forces like gravity or the Coriolis force. Such motion may irreversibly dissipate into friction. Thus, at least in a thermodynamic sense, high entropy can be understood as a prerequisite for motion in the form of large-scale eddies which, at the end of the scale cascade, may drive turbulent mixing (see f g. 2.7).

Thus, we identify the entropy of each air parcel, $S_{ap} = \Delta S$, with the ability to transform ΔS into work. Within the framework of thermodynamics, this can be done in the idealized Carnot cycle (see f g. 2.7) where the area of the red dashed rectangle (right panel) describes the maximal

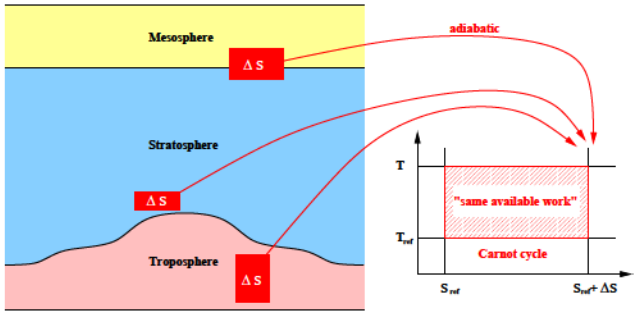

Figure 2.7: The air parcels with different volumes V_{ap} but with the same amount of entropy $S_{ap} = \Delta S = V_{ap}s$ (s is given by (2.20)) are adiabatically transformed into a state with the same temperature T (note that although having the same temperature, these air parcels differ in their pressures and number of molecules). These air parcels, if included in the Carnot cycle working between the temperatures T and T_{ref} ($T > T_{ref}$) and entropies S_{ref} and $S_{ref} + \Delta S$, would transform heat into the same amount of available work (red dashed rectangle). In the atmosphere, such work is manifested as large-scale eddies which may drive mixing. In a system with no additional information, this criterion def nes air parcels with the "same potential for mixing".

amount of available work done along the isothermal-isentropic branches of the Carnot cycle (i.e. $W = \Delta T \Delta S$, $\Delta T = T - T_{ref}$). During this cycle, heat is transported from the warmer reservoir with temperature T to the colder reservoir with temperature T_{ref}.

An example of how to realize such processes in the real atmosphere is the transport of heat by breaking small-scale planetary or gravity waves. Thus, although waves themselves can be considered as adiabatic processes with $\theta = \text{const}$, the breaking of such waves and the associated mixing are diabatic and non-conservative. E.g., breaking planetary waves which drive the Brewer-Dobson circulation, transport heat from the tropics to the extratropics. Another example is gravity waves which break due to some shear instabilities in the f ow. Thus, if nothing else is known about the system, the same entropy of the air parcels means the "same likeliness" that such irreversible transport may happen.

In a Lagrangian transport scheme where each mixing event is parametrized by the numerical diffusion resulting from the (adaptive) re-gridding procedure, it is necessary to cover the whole atmosphere with the "same accuracy" with respect to the "resolution of mixing". This means that only a few air parcels are necessary in regions with strong mixing (e.g. the well-mixed lower troposphere) whereas f ow domains with weak mixing and high spatial variability of transported species require more air parcels (e.g. the stably stratif ed lowermost stratosphere).

Thus, we propose a distribution of air parcels over the entire atmosphere by using the weighting def ned by the entropy s. We f x the entropy of each air parcel, S_{ap}, by

$$S_{ap} = V_{ap}s(\theta, \rho), \tag{2.21}$$

with the air parcel volume, $V_{ap} = r^2 \Delta z$, and the entropy density s given by eq. (2.20). Note that $n_{ap} = 1/V_{ap}$ describes the number density of air parcels. Assuming $S_{ap} = \text{const}$ and s being prescribed via eq. (2.20), an implicit relation for r and Δz can be derived from eqs. (2.20) and (2.21). This relation is our first condition on how to select the parameters r and Δz. But we need also a second condition.

Here, we follow the assumption that the aspect ratio $\alpha = r/\Delta z$ is related to the static stability $d\theta/dz$. Static stability can be quantified in terms of the Brunt-Vaisala frequency $N^2 = (g/\theta)(d\theta/dz)$. N describes the frequency at which an air parcel oscillates when displaced vertically in a statically stable environment, i.e. within a region with $d\theta/dz > 0$. Because the well-mixed troposphere is characterized by low values of N and the stably stratified stratosphere by high values of N, it is expected that this difference also will also be manifested in the corresponding vertical diffusivities (large and small for the troposphere and the stratosphere, respectively), and consequently, in the related aspect ratios.

Even a linear relation can be expected between α and N. The motivation for this assumption follows from the geostrophic approximation of the horizontal momentum equation governing the spatial and temporal distribution of the extratropical winds (*Andrews et al.*, 1987). Assuming that typical scales of dynamical variability driven by the Coriolis force can be quantified by the (horizontal) Rossby radius and by the vertical extension of the corresponding lens of the disturbed air, the relation $\alpha = N/f$ can be derived with $f = 2\Omega \sin(\phi)$ denoting the Coriolis parameter (Ω-rotation rate of the Earth, ϕ-latitude) (*Lindzen and Fox-Rabinovitz*, 1989).

Motivated by such deliberations, we formulate our second main assumption

$$\alpha = f(N) = kN, \tag{2.22}$$

with $k = \alpha_0/N_0 = \text{const}$ describing a linear dependence of the aspect ratio α on N. We assume $\alpha_0 = 250$ and $N_0^2 = 4.0 \cdot 10^{-4}\ \text{s}^{-2}$, i.e. α_0 is the expected aspect ratio in the lower stratosphere around $\theta = 380$ K (*Haynes and Anglade*, 1997) and N_0^2 can be estimated from the US standard atmosphere on the same θ-level (see fig. 2.6).

Consequently, r and Δz follow from the following two equations:

$$\frac{1}{r^2 \Delta z} = \frac{s}{S_{ap}}, \qquad \frac{r}{\Delta z} = kN \tag{2.23}$$

and, after some reformulation, are given as

$$r = \left(\frac{kNS_{ap}}{s} \right)^{\frac{1}{3}}, \qquad \Delta z = \left(\frac{1}{kN} \right)^{\frac{2}{3}} \left(\frac{S_{ap}}{s} \right)^{\frac{1}{3}} \tag{2.24}$$

Furthermore, we slightly re-formulate the condition $S_{ap} = \text{const}$ as

$$S_{ap} = r_0^2 \Delta z_0 s_{max} = \frac{r_0^3}{\alpha_0} s_{max} \tag{2.25}$$

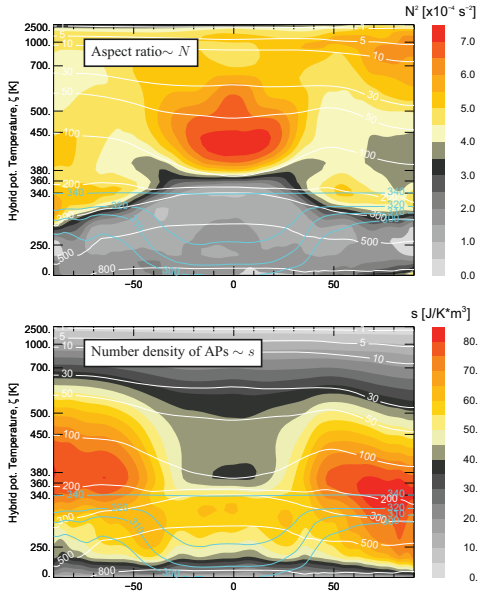

Figure 2.8: Zonally averaged values of the Brunt-Vaisala frequency N^2 (top) and the entropy density s with θ_0 def ned by θ on the Earth's surface (i.e. $\theta_0 = \theta_0(\lambda, \phi)$ λ/ϕ - longitude, latitude). All the distributions are from the ECMWF ERA-Interim re-analysis on January 1, 2008, 12 UTC. $\Delta\zeta$ was interpolated from Δz by using the hybrid coordinate ζ (*Mahowald et al.*, 2002) and the geopotential from the ECMWF ERA-Interim re-analysis. The blue and white lines are potential temperature and pressure levels. For the calculation $r_0 = 100$ km and $\alpha_0 = 250$ (i.e. $\Delta z_0 = 400$ m) and $k = \alpha_0/N_0$ with $N_0^2 = 4.10^4\ s^{-2}$ was assumed.

with r_0 being the prescribed value of r at maximum entropy density s given by s_{max} (thus, assuming $\alpha_0 = 250$, the choice of r_0 def nes S_{ap}). Hence, prescribing r_0 at the level of the maximum entropy s_{max} f xes the horizontal and vertical resolution r and Δz throughout the atmosphere (eqs. (2.24).

A 3D generalization of this concept uses 3D f elds of N and s derived from the meteorological data. An example is shown in f g. 2.8 showing the zonal averages calculated from the ECMWF ERA-Interim re-analysis for the January 1, 2008, 12 UTC. Note that because of the linearity of eqs. (2.23), N represents the spatial distribution of the geometric aspect ratio def ned as $\alpha = r/\Delta z$ and s describes the volume density of the air parcels, $n_{ap} = (r^2\Delta z)^{-1}$. Thus, the largest geometric aspect ratios are expected in the tropics well above the tropical tropopause and the "densest" coverage of such grid points has to be expected in the lower polar stratosphere. If each air parcel contained the same mass, the corresponding volume density would follow the air mass density with the highest values at the Earth's surface and with a strong exponential decrease with altitude.

In summary, the entropy and stability-based scales provide a framework for generating a grid in which the numerical diffusion associated with interpolations due to re-gridding would properly scale. The most important properties of such a grid are shown schematically in f g. 2.9. Thus, above the tropopause, mainly in regions with enhanced N, the grid of air parcels is def ned by large values of α, thus minimizing the vertical diffusivity because of the smallest vertical extension of such air parcels. On the other hand, tropospheric air parcels, or air parcels in the upper stratosphere are characterized by much smaller values of α with larger vertical scales

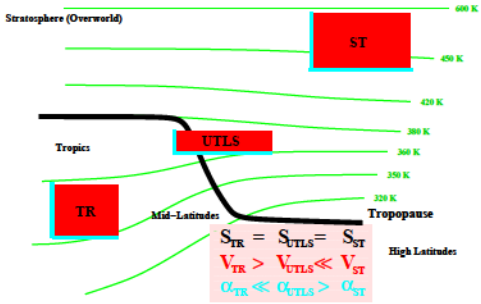

Figure 2.9: Entropy and static stability-based scales which uniformly cover the whole atmosphere. s, V, and $\alpha = r/\Delta z$ denote the entropy, volume and the aspect ratio of three representative air parcels in the troposphere (TR), stratosphere (ST) and in the vicinity of the tropopause (UTLS), respectively.

enhancing the vertical numerical diffusion. In addition, the highest density of air parcels, which is a consequence of the entropy criterion, has to be expected above the tropopause in the polar lower stratosphere (f g. 2.8 bottom), i.e. in regions where strong f lamentary structures are formed by the chaotic advection driven by the jets.

2.6 Re-gridding procedure

As discussed at the end of section 2.4, Lagrangian transport offers a two-step procedure how to implement physical mixing into a transport scheme so that numerical diffusion mimics rather than disturbs the physical diffusivity. After def ning an appropriate grid in the previous section (f rst step), the question arises which physical processes trigger mixing in the atmosphere and how such processes can be numerically implemented into the transport scheme using grid interpolations or, in other words, by using an appropriate re-gridding scheme (second step).

Our heuristic idea for def ning a mechanism triggering mixing events is to identify regions in the atmosphere which are "unstable" and which may undergo "strong deformations". The f ow is called unstable if a small perturbation at initial time will grow signif cantly during the course of the evolution of the f ow. From the Lagrangian perspective, this mean that the distance between the adjacent air parcels increases "suff ciently fast". Thus, by monitoring this property in the Lagrangian grid it is possible to detect such regions in the f ow and, subsequently, by re-gridding these parts of the grid, to trigger numerical diffusion through the related interpolations.

A further motivation is based on the gradient Richardson number, i.e. on a dimensionless critical ratio Ri_c describing the onset of instabilities driven by wind shear and/or buoyancy (*Turner*, 1973). Ri is def ned as

$$Ri = \frac{N^2}{\left(\frac{\partial u}{\partial z}\right)^2 + \left(\frac{\partial v}{\partial z}\right)^2} \tag{2.26}$$

with u, v denoting the horizontal wind components and N the Brunt Vaisala frequency. Ri_c, is about 0.25 (although reported values have ranged from roughly 0.2 to 1.0) with the f ow becoming dynamically unstable or even turbulent when $Ri < Ri_c$. Such turbulence occurs either when

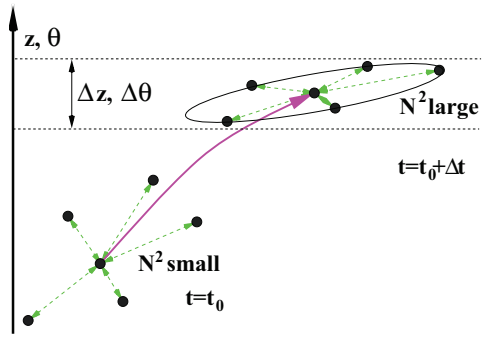

Figure 2.10: Mixing driven by the (wet) static stability. If $N^2 = (g/\theta_e)d\theta/dz$ (θ_e - equivalent potential temperature) is small or even negative - a state that may occur mainly in the troposphere - effective (vertical) mixing is expected. In the Lagrangian parametrization, the mixing ratios of the affected air parcel and its next neighbors are set to their average value. Such regions can be diagnosed from a sufficiently large change of the vertical separation between the next neighbors during the advection step and should correlate with vertically unstable or weakly stable regions (small values of N^2).

the wind shear is great enough to outweigh any stabilizing buoyant forces (denominator is large), or when the dry or, more general, moist environment is statically unstable (numerator is small or even negative).

In the Lagrangian realization of this concept, the local shear rates in the flow have to be replaced by the integral deformation which can be derived from the relative motion of the next neighbors occurring during the Lagrangian time step Δt (see below). In addition, in the troposphere, where the (wet) static stability N^2 can be small, the weakly stratified or the unstable regions of the atmosphere can effectively drive vertical mixing (see fig. 2.10). In contrast, in the stratosphere, where the flow is characterized by high static stability, only sufficiently strong, almost horizontal deformations are expected to drive mixing within the considered stratospheric layer.

In the following, we show how the mixing scheme of the Chemical Lagrangian Model of the Stratosphere (CLaMS) implements the concept of deformation-induced mixing in a Lagrangian grid (*McKenna et al.*, 2002; *Konopka et al.*, 2004, 2007) (see fig. 2.3 and fig. 2.11, top panel). Here, the critical deformation γ_c is defined as $\gamma_c = \Delta t \lambda_c$. λ_c denotes the 2D finite-time critical Lyapunov exponent describing a deformation of a sufficiently small circle with a radius r_0 into an ellipse with major and minor axes given by $r_\pm = \exp \pm \lambda_c \Delta t$ (appendix A.5). At first, both the time step Δt and λ_c are free parameters.

In order to decide whether a deformation occurring in the real atmospheric flow surrounding a given air parcel exceeds γ_c, its next neighbors within a layer of thickness Δz (or $\Delta\theta$ as shown in the top panel fig. 2.11) are calculated by means of the 2D Delaunay triangulation described in appendix A.6. This is done before the advection step. Furthermore, let us assume that the mean distance of the considered air parcel to the next neighbor is given by the mean separation between the air parcels in the considered layer, i.e. by $r = r_0$. Then, during the advection step, both horizontal deformations (mainly strain) and vertical deformation within the almost horizontal

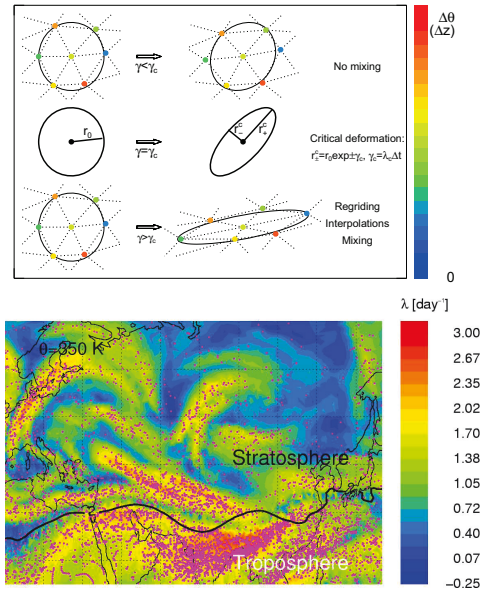

Figure 2.11: Deformation-induced mixing in CLaMS. Top: Mixing parameters (from (*Konopka et al.*, 2005b)). The CLaMS mixing algorithm is triggered if during the advection step Δt the relative positions between the next neighbors within a layer with thickness Δz (or $\Delta\theta$) changes with a suff ciently high rate $\gamma > \gamma_c$. For $\gamma < \gamma_c$ mixing-free transport occurs along the trajectories. Bottom: Realization of mixing (from (*Pan et al.*, 2006)). Finite-time Lyapunov exponent λ describing integral deformation at $\theta = 350$ K. Highest values of λ can be diagnosed in the vicinity of the jet separating the troposphere from the stratosphere (black line, PV=2). Mixing algorithm in CLaMS yields the highest mixing rates due to the largest number of interpolations carried out in the region with the highest values of λ (pink dots denote the new air parcels inserted into the scheme).

layer (mainly shear) change the relative positions of the next neighbors.

After the advection step, the distances r to the next neighbors are compared with those before the advection step. If r exceeds r_+, a new air parcel is included in between with the mixing ratio of the transported species linearly interpolated from the air parcels for which $r > r_+$ was diagnosed. In order to keep the mean separation between the air parcels per layer within certain bounds (here around r_0), renewed triangulation allows the distances to the current next neighbors to be checked and the redundant air parcels are removed by means of the same linear interpolations (i.e. two air parcels are replaced by one in the middle). In CLaMS, the criterion $r < r_-$ is used for the redundant air parcels but variations of this condition are possible (*Wohltmann and Rex*, 2009). Note that the linear interpolations used for calculating the mixing ratios of new air parcels are essential, because, assuming similar volumes of the interacting air parcels, such

interpolations mimic fully mixed states of the air parcels involved.

An example of this procedure is shown in the bottom panel of fig. 2.11 where new air parcels inserted into the grid around $\theta = 350$ K are highlighted (pink dots). The finite-time Lyapunov exponent λ is color-coded, which is calculated from the deformation of 3D circles (i.e. distributed around each air parcel within the layer). Around PV=2 (black line) a strong jet over the Himalayas can be diagnosed forming a sharp isentropic transport barrier between the stratosphere and the troposphere. A clear correlation between λ and the number of new air parcels shows how deformation-induced mixing works in CLaMS (i.e. for a given advective time step Δt deformations with $\lambda > \lambda_c$ trigger the re-gridding procedure).

Note that because a layer concept is used in CLaMS in order to determine the next neighbors, deformations with a strong change of the vertical distance between the next neighbors (e.g. during convection events) cannot be detected with this scheme (for possible extension see caption in fig. 2.10). Nevertheless, a strong inhomogeneity of Lagrangian mixing, both in time and space (according to CLaMS less than 15% of air parcels per day are affected by mixing), is the most pronounced difference to the Eulerian approach where numerical diffusion is ubiquitous.

2.7 Closing remarks

Lagrangian transport in CLaMS stands for the possibility to replace the numerical diffusion by physical mixing. Starting from the idealized case with no mixing, i.e. from transport that is only driven by trajectories, a mixing parametrization can be gradually included in the scheme. Thus, in contrast to the Eulerian schemes, mixing can be tuned from zero to an arbitrary value that renders sensitivity studies possibly, e.g. in order to study the impact of mixing on transport, chemistry or microphysics (see e.g. *Konopka et al.*, 2003b,a, 2005a).

Grid definition, its resolution or the critical deformation γ_c are parameters defining the intensity of mixing. These parameters can only be fixed by comparison with experimental data. For example, *Konopka et al.* (2004) and *Wohltmann and Rex* (2009) describe how tracer-tracer correlation and time series of tracers observed in situ confine the possible values of the mixing parameters in the models CLaMS or ATLAS. Here, a combined metric of a "smallest deviation" in tracer-tracer and in the physical space is defined in such a way that the model optimizes both the curvature of the non-linear F11-O_3 correlation and the variability of the observed time series of CH_4. If satellite observations with their coarse spatial resolution and associated optical mixing are used, the curvature of the non-linear tracer-tracer correlations is not well reproduced. In such a case, the use of PDFs instead of the tracer-tracer correlations is more justified (*Konopka et al.*, 2005b).

3 Scientif c achievements: Composition of air in the UTLS region

The aim of this chapter is to work out the key points of all publications relevant for this "kumulative Habilitationsschrift", especially in context of the stage of our knowledge based on literature. The outline follows the short description given in the introduction.

In the following, we use the multi-annual CLaMS simulations covering 35 years (from 1979 to 2014) with the model transport driven by the European Centre for Medium-range Weather Forecasts (ECMWF) meteorological ERA-Interim reanalysis (*Simmons et al.*, 2006; *Uppala et al.*, 2008; *Dee et al.*, 2011). In the stratosphere, the potential temperature θ is employed as the vertical coordinate of the model and the cross-isentropic velocity $\dot{\theta}$ is deduced from the ERA-Interim forecast total diabatic heating rate, including the effects of all-sky radiative heating, latent heat release and diffusive heating as described in *Ploeger et al.* (2010). In the troposphere, the vertical model coordinate smoothly transforms into an orography-following σ-coordinate, with the vertical velocity transforming into the corresponding $\dot{\sigma}$ (*Mahowald et al.*, 2002).

The specif c model setup employed here closely follows the CLaMS conf guration described by *Konopka et al.* (2010) with a vertical and horizontal resolution in the UTLS region of about 400 m and 100 km, respectively. *Pommrich et al.* (2014) summarizes the chemistry used in these simulations.

3.1 Asian summer monsoon and the seasonality of tropical ozone in the lower stratosphere

The annual cycle of the composition of air in the upper troposphere lower stratosphere (UTLS) region is determined by the seasonality of different transport processes such as convection, Brewer-Dobson (BD) circulation and two-way irreversible isentropic transport (*Holton et al.*, 1995; *Fueglistaler et al.*, 2009; *Gettelman et al.*, 2011). Signif cant hemispheric differences of all these transport processes result from the hemispheric asymmetry of the land-sea distribution and the orography.

Based on multi-annual simulations with CLaMS, *Konopka et al.* (2015) discuss hemispheric

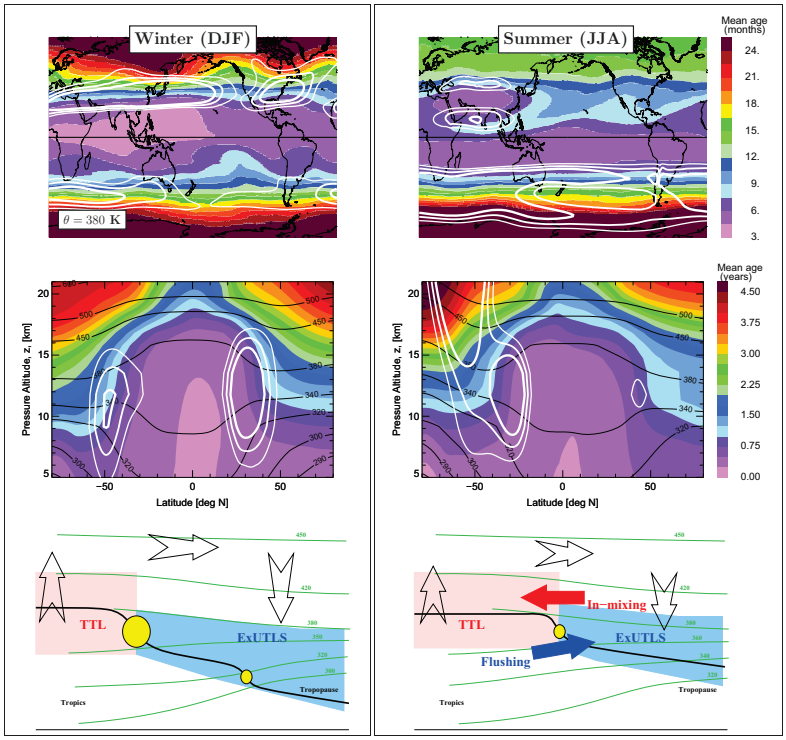

Figure 3.1: The seasonality of mean age of air, winter (DJF, left column) versus summer (JJA, right column) at $\theta = 380$ K (top row), as a zonally averaged distribution (middle row) and with a schematic explanation of the most important differences (bottom row). The isolines of wind (white, 20, 25, 30 m/s from thin to thick, respectively) illustrate the positions of the jets (partially adapted from *Konopka et al.* (2015)).

asymmetries and the seasonality of the mean age of air in the lower stratosphere (f g. 3.1). For example, at $\theta = 380$ K (top panel of f g. 3.1) the air masses in the southern polar hemisphere are much older than the air masses in the northern polar hemisphere during summer (note that for an aqua-planet these distributions should be equal).

This asymmetry can also be diagnosed in the zonally averaged vertical cross sections of mean age of air shown in the middle panel of f g. 3.1: during the same season, air is always younger in the NH than in the SH. A similar hemispheric asymmetry exists in the zonal wind distributions (white contours). In the winter hemispheres, the subtropical jet forms a strong transport barrier between the tropics and extratropics and the polar jet separates mid- and high latitudes in the extratropics. On the other hand, these barriers weaken signif cantly in the summer hemispheres, most pronouncedly in the NH (*Haynes and Shuckburgh*, 2000a,b).

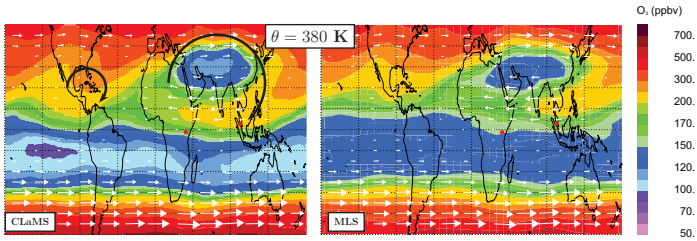

Figure 3.2: The summer (JJA) distribution of O_3 at $\theta = 380$ K calculated with CLaMS (left) and observed by MLS (right). The young tropospheric air convectively lifted to this altitude is characterized by very low values of O_3. The STE manifests itself in (isentropic) mixing of the young (tropospheric) air within the core of the monsoon anticyclone, typically also containing enhanced values of CO, HCN (not shown), with old stratospheric air in its outer f anks (high O_3) and the subsequent, almost isentropic, transport of these air masses into the TTL (adapted from *Konopka et al.* (2010)).

Furthermore, the upward f ux of air into the stratosphere is not zonally symmetric, as can be inferred from the comparison of mean age of air in the tropics at $\theta = 380$ K (top panel of f g. 3.1). The youngest air can therefore be diagnosed in winter above the West Pacif c warm pool whereas in summer the Asian summer monsoon anticyclone forms the key pathway for transport into the stratosphere (*Dethof et al.*, 1999; *Randel and Park*, 2006; *Randel et al.*, 2010). This nearly stationary summer circulation extends well into the lower stratosphere up to about 18 km (or θ =420 K) and effectively isolates the air masses of tropospheric origin inside from the much older, mainly stratospheric air outside this anticyclone (*Park et al.*, 2008).

Konopka et al. (2015) show that poleward of 60° the main reason for hemispheric differences in the age of air distribution are because eddy mixing in the NH outweighs that in the SH throughout the year. *Konopka et al.* (2015) also show that in the tropical lower stratosphere between ±30°, the air becomes younger during boreal winter and older during boreal summer. During boreal winter, the decrease of age of air due to tropical upwelling outweighs aging by isentropic mixing. In contrast, weaker isentropic mixing outweighs an even weaker upwelling in boreal summer and fall making the air older during these seasons.

The impact of this effect on the seasonality of ozone with its pronounced maximum during summer and fall (see e.g. *Randel et al.* (2007a) and references therein) was investigated in my previous studies (*Konopka et al.*, 2009, 2010; *Ploeger et al.*, 2012). Fig. 3.2 shows the climatological summer distribution of O_3 at $\theta = 380$ K derived from the CLaMS simulations (left) and observed by the Microwave Limb Sounder (MLS) on the NASA Earth Observing System (EOS) Aura (*Schoeberl et al.*, 2006) (right). The similarity of the patterns between MLS and CLaMS, with a clear signature of the Asian monsoon anticyclone, conf rms the seasonality of transport resolved by CLaMS.

An obvious feature that can be derived from this comparison is that the Asian monsoon an-

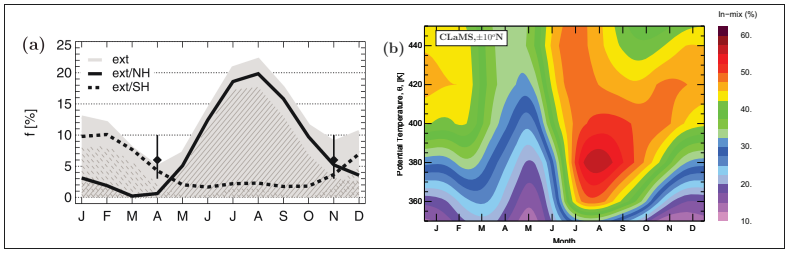

Figure 3.3: The seasonality of in-mixing from the extratropics into the TTL (tropics: $\pm 10^{\circ}$N, extratropics: $> |30|^{\circ}$N eq. latitude). (a) in-mixed air in the northern/southern hemisphere (black/dashed) and total (gray, adapted from *Ploeger et al.* (2012)). (b) in-mixed O_3 (adapted from *Konopka et al.* (2009)).

ticyclone seems to drive in-mixing of ozone (O_3), i.e. enhanced equatorward transport from the extratropics into the upper part of the TTL (i.e. above $\theta \approx 370$ K), which may have a signif cant effect on the seasonality of the tropical O_3. More precisely, the question arises of the percentage of the in-mixed air and O_3 in relation to the total tropical air and O_3, respectively.

Konopka et al. (2009) and *Ploeger et al.* (2012) answer these questions using backward trajectories driven by ECMWF ERA-Interim winds and a conceptual one-dimensional model of the chemical composition of the TTL. The results shown in f g. 3.3 verify a strong seasonality of in-mixing with the highest in-mixing rates during summer. Note that the maximum of in-mixed air of around 20% translates into around 50% of in-mixed O_3 due to strong meridional gradients of O_3. Furthermore, this eddy-driven, large-scale isentropic transport of O_3 (in the zonal mean, this transport can be understood as eddy mixing) is decoupled from the mass transport of the residual circulation in agreement with the results of *Yang et al.* (2008), who found that during boreal summer the upward mass f ux in the tropics has a near-zero minimum around 70 hPa.

Finally, *Abalos et al.* (2013) reconcile the recently published, apparently contrasting results regarding the relative importance of tropical upwelling versus horizontal transport for the seasonality of ozone above the tropical tropopause. Different analysis methods in the literature (Lagrangian versus Eulerian, and isentropic versus pressure vertical coordinates) yield different perspectives of ozone transport, and the results must be carefully compared in equivalent terms to avoid misinterpretation.

Fig. 3.4 shows the seasonality of in-mixing, presented as its net effect on tropical ozone tendency (relative to the annual mean ozone mixing ratio), as a function of isentropic levels. In order to compare the Lagrangian and Eulerian frameworks, we contrast results from the WACCM (Whole Atmosphere Community Climate Model, *Garcia et al.* (2007)) chemistry climate model with results from the conceptual Lagrangian one-dimensional model as used in *Ploeger et al.* (2012).

Again, we note that the magnitude and exact levels are not expected to be comparable, and

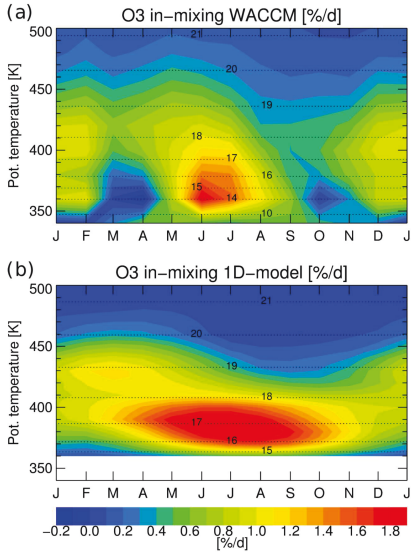

Figure 3.4: Vertical structure of the seasonal cycle in in-mixing of ozone into the tropics (±20N). Shown is the in-mixing contribution to the ozone tendency relative to the annual mean ozone concentration in [% day^{-1}], from WACCM (Eulerian view, (a)) and from the 1-D model (Lagrangian view, (b)) (adapted from *Abalos et al.* (2013)).

only broad characteristics should be considered. The seasonality of in-mixing shows a common feature in both models: there is strong in-mixing of ozone during the NH summer limited to isentropic levels below 420 K, while at higher levels both models experience slightly more in-mixing in boreal winter-spring compared to summer-autumn. In both models, the strong maximum is clearly identif ed in the ozone in-mixing during boreal summer at levels around the tropical tropopause, which is associated with the monsoons. The vertical extension of this summer maximum is larger in WACCM, while in the 1-D model the maximum is broader in time. Notwithstanding these differences, both models show this maximum and a consistent transition to a smaller seasonality at higher altitudes.

3.2 Mixing-driven origin of the Extratropical Transition Layer (ExTL) and of the Tropopause Inversion Layer (TIL)

The Extratropical Transition Layer (ExTL) is a subset of the ExUTLS discussed in f g. 1.1 (*WMO*, 2003; *Gettelman et al.*, 2011). Motivated by in situ observations of CO-O_3 correlations, the most convenient way to def ne the ExTL is to separate the mixed air parcels in the CO-O_3 space from pure tropospheric and pure stratospheric branches using the criteria discussed in *Pan et al.* (2010) (see f g. 3.5). The ExTL can be understood as a result of the isentropic

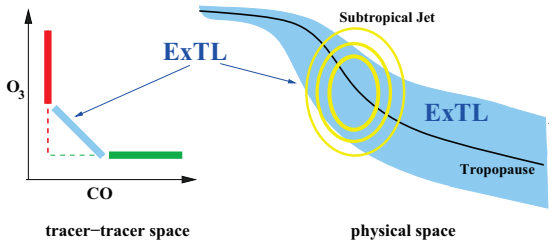

Figure 3.5: In the CO-O_3 space (left), the ExTL is def ned as a mixed part (blue) that deviates from the idealized, L-shape correlation (dashed) consisting of a pure tropospheric (green) and a pure stratospheric (red) branch. The position of the respective air parcels in physical space (right) def nes the geometric position, in particular the vertical extension of the ExTL (*Pan et al.*, 2007, 2010).

two-way transport above or below the subtropic and polar jets that is mainly driven by the barotropic (above the jets) and baroclinic (below the jets) Rossby waves (*Holton et al.*, 1995; *Polvani and Esler*, 2007; *Homeyer and Bowman*, 2012) and become apparent in different forms of stratosphere-troposphere exchange (STE) such as deep intrusions or tropopause folds (see f g. 3.6).

Because (non-breaking) Rossby waves, like all other periodic disturbances, are *per se* reversible, the question arises of when such processes lead to an irreversible STE forming the ExTL, i.e. to a mixed branch of the CO-O_3 correlation discussed in f g. 3.5. Since mixing is an accumulative process integrating in time, the observed time series of the chemical composition alone does not provide direct evidence of when and where the relevant mixing events took place. However, CLaMS that explicitly resolve mixing (see bottom left panel of f g. 3.6) allow the signatures of mixing observed in the CO-O_3 correlations to be related to the f ow conf gurations upstream. In particular, freshly mixed air parcels on a time scale of several days can be separated from those air parcels which have a much older mixing history (*Konopka and Pan*, 2012).

Starting from an idealized ExTL with a perfectly segregated troposphere and stratosphere (this can be done in the model by initializing CO and O_3 according to the idealized L-shape correlation shown in f g. 3.5), we quantify the time scale of ExTL formation by evaluating the length of time it takes for the model transport process (advection + mixing) to reproduce the observed features of the ExTL (see also f g. 3.7). We found that the shortest time scales of ExTL formation are on the isentropic levels below the subtropical jet core, e.g. around 3 weeks for 310 K, whereas at the 360 K level (where the ExTL intersects the jet core) it is around 3 months. Much longer times are required to form ExTL at the 360 K level ref ecting that mixing is prohibited in the region of the jet core.

We have also found that the longest (shortest) time scales for the formation of the ExTL are diagnosed in regions with high (low) values of the Brunt-Vaisala frequency N^2 (green and orange lines in f g. 3.7). The largest differences between these two parts were found for isentropes crossing the jet, i.e. for θ between 320 and 360 K. This means that the tropopause inversion layer (TIL, *Birner et al.* (2002)) characterized by large values of N^2 needs signif cantly more

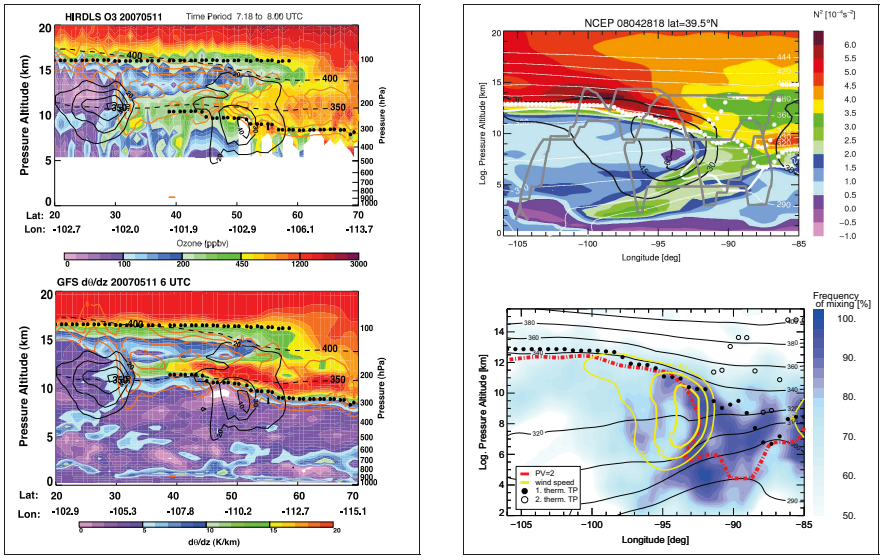

Figure 3.6: Left: Deep tropospheric intrusion of low ozone from the tropics into the high latitudes as observed on May 5, 2007, with the HIRDLS instrument (top) and the static stability $d\theta/dz$ derived from the meteorological data (bottom). The GFS analysis thermal tropopause (black dots), zonal wind (black contour), 350 and 400 K isentropes (black dashed), and PV (2, 4, 6, and 8 PVU) contours are also shown on the cross sections (adapted from *Pan et al.* (2009)). Right: The tropopause fold sampled on April 28, 2008 from the research aircraft Gulfstream V (f ight track colored gray) can be clearly seen in the vertical cross section of the Brunt-Vaisala frequency N^2 derived from the meteorological data (top, adapted from *Vogel et al.* (2011)). The frequency of mixing derived from CLaMS quantif es the number of mixing events experienced by the air in the last 3 days (bottom). The NCEP thermal and dynamical tropopause, zonal wind and the isentropes are also shown (adapted from *Konopka and Pan* (2012)).

time to be fully reconstructed from our idealized experiment.

Randel et al. (2007b) suggested that the radiative effects of both O_3 and H_2O near the tropopause may make a substantial contribution to the formation and maintenance of the TIL. It has also been proposed that other mechanisms contribute to TIL formation. *Birner* (2006) argued that the TIL could be the result of poleward heat f uxes together with extratropical baroclinic eddies. *Wirth* (2003, 2004) suggested that the asymmetry between upper-level cyclones and anticyclones and their effects on the local stratif cation around the tropopause is responsible for the existence of a TIL in the climatological mean. Balanced dynamics studies by *Wirth and Szabo* (2007) revealed enhanced N^2 in the lower stratosphere as a feature of anticyclonic upper tropospheric f ow.

Thus, the question arises of whether the formation of the TIL is a process occurring on synoptic scales (balanced dynamics) or on seasonal scales (radiation) or, as recently suggested

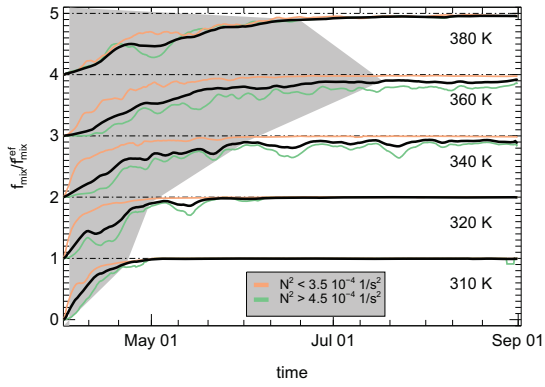

Figure 3.7: Formation of the ExTL at $\theta = 310, \ldots 380$ K in spring and summer in the northern hemisphere. The respective time scales can be estimated from the condition $f_{mix}/f_{mix}^{ref} = 0.9$ meaning that the CLaMS ExTL reproduced from the L-shape initialization is almost the same (i.e. up to 10%) as that known from the observations (for better visibility, the black curves are shifted along the y-axis). In this way, the gray area quantif es the time scales of formation of the ExTL relative to the initialization time (here: April 1, 2008). By def ning two different subsets of the ExTL, with large and small values of N^2 (green and orange), the impact of the stability on the formation of the ExTL can also be inferred (adapted from *Konopka and Pan* (2012)).

(*Birner*, 2010), the combination of different physical mechanisms drives the formation of the TIL. (*Birner*, 2010) also argue that such a combination of different physical mechanisms may strongly depend on the geographical position and on the season.

Our analysis shows that the TIL is a part of the ExTL, i.e. of a well-mixed transition layer containing both tropospheric and stratospheric signatures, in particular relatively high mixing ratios of water vapor (*Kunz et al.*, 2009). Following *Kunz et al.* (2009) the TIL consists of air parcels with "old" or "frozen-in" mixing, which took place on a seasonal rather than a synoptic time scale. *Kunz et al.* (2009) emphasized that a necessary condition for this effect is a well-mixed ExTL where relatively high water vapor (up to 30 ppmv) coexists with high ozone (up to 300 ppbv, see f g. 3.8).

Fig. 3.8 also illustrates the results of the f xed dynamical heating (FDH) calculations showing that the TIL vanishes for an idealized case of non-mixed prof les, i.e. for perfectly segregated tropospheric and stratospheric reservoirs. This, in turn, leads to the conclusion that the radiative mechanism inherently includes transport, in particular mixing effects, by assuming that the STE leads to the observed O_3 and H_2O distributions. Furthermore, these results also suggest that H_2O rather than O_3 plays a major role in maintaining the temperature inversion (*Kunz et al.*, 2009).

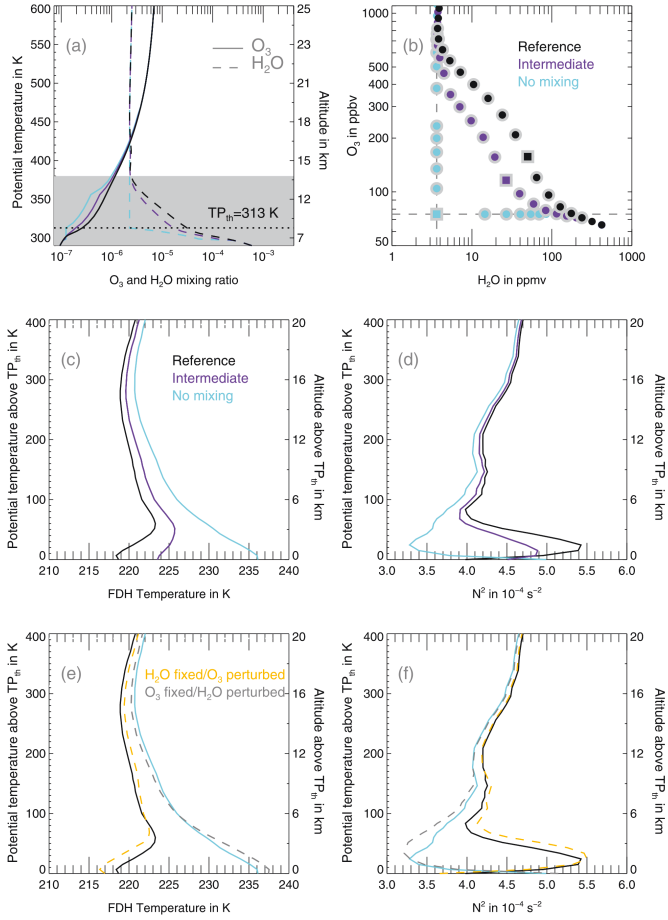

Figure 3.8: (a, b) ECMWF mean vertical profiles of O_3 (solid lines) and H_2O (dashed lines) at 60°N relative to different states of the atmosphere, i.e., non-mixed (cyan), mixed (black), and intermediate case (purple). (c, d) Based on fixed dynamical heating (FDH) calculations, resulting temperature profiles and the static stability N^2 for the different mixing states. (e, f) The FDH calculations if one of the two trace gases is kept constant: O_3 (gray dashed) or H_2O (yellow dashed) (adapted from *Kunz et al.* (2009)).

Note that the bi-directional STE processes are mixing processes across the ExTL or, in other words, stratosphere-ExTL-troposphere exchange processes (S-ExTL-T) with S and T denoting pure stratosphere and troposphere, respectively. Because of the considerable thickness of the ExTL (up to a few kilometers (e.g. *Hoor et al.*, 2004)), the residence times of the air parcels in such "no-man's land" are of the order weeks to months.

Thus, diagnosing the net transport of trace gases such as ozone from the (pure) stratosphere to the (pure) troposphere or vice versa, i.e., the net stratosphere-to-troposphere (STT) or troposphere-to-stratosphere (TST) tracer transport, must take into account the existence of this layer (which is, of course, different from the mathematical surface def ning the tropopause). This is a different manifestation of the concept that the transport of mass is driven only by the f ow velocity (and can therefore be diagnosed in terms of pure trajectory calculations) whereas, in addition to this advective f ux, the gradient-driven and species-dependent diffusive f uxes (i.e., mixing) determine tracer transport across the tropopause.

3.3 Climatological relevance of mixing and interpretation of trends

The UTLS region plays an important role in the climate system. Changes in the structure and chemical composition of this region result in particularly large changes in radiative forcings of the atmosphere (see f g. 1.2). As discussed in *Riese et al.* (2012), there is a strong inf uence of uncertainties in the atmospheric mixing strength on global UTLS distributions of greenhouse gases, especially of water vapor and ozone, and associated radiative effects. To quantify these uncertainties CLaMS simulations were applied with different, but physically reasonable mixing intensity ("reasonable mixing" means in this context that the degree of agreement of such sensitivity studies with observations is "almost" the same).

The inferred uncertainties are large. For water vapor and ozone, annual mean globally averaged radiative forcing effects of 0.72 and 0.17 W/m^2 were found, respectively (*Riese et al.*, 2012). For comparison, changes of the radiative forcing since 1980 due to well-mixed greenhouse gases, aerosols, and stratospheric water vapor are of the order of 1.0 W/m^2 (*Solomon et al.*, 2010). *Solomon et al.* (2010) derived the impact of this radiative forcing change on global surface temperature and found a value of about 0.4 K. For ozone, the radiative effect of mixing uncertainties mainly results from changes in the stratosphere. The effect is as large as about 40% of the total anthropogenic tropospheric ozone forcing (*Solomon et al.*, 2007). The radiative effect of stratospheric ozone due to mixing uncertainties is the most reliable result of our simulations, because transport and mixing in the stratosphere are particularly well represented in CLaMS and changes in ozone are not correlated with changes in clouds (*Riese et al.*, 2012).

The lack of a quantitative understanding of STE may also inf uence the interpretation of the observed atmospheric trends, in particular of those sampled in the troposphere as the following example illustrates. Based on ozonesonde measurements, *Wang et al.* (2012) report on the O_3 seasonality over Beijing, which shows a winter minimum and a broad summer maximum (see panel (a) in f g. 3.9).

In addition, a pronounced summer ozone maximum between 0 and 2 km can be diagnosed in the observations, which results from pollution-driven O_3 formation, mainly as a consequence of

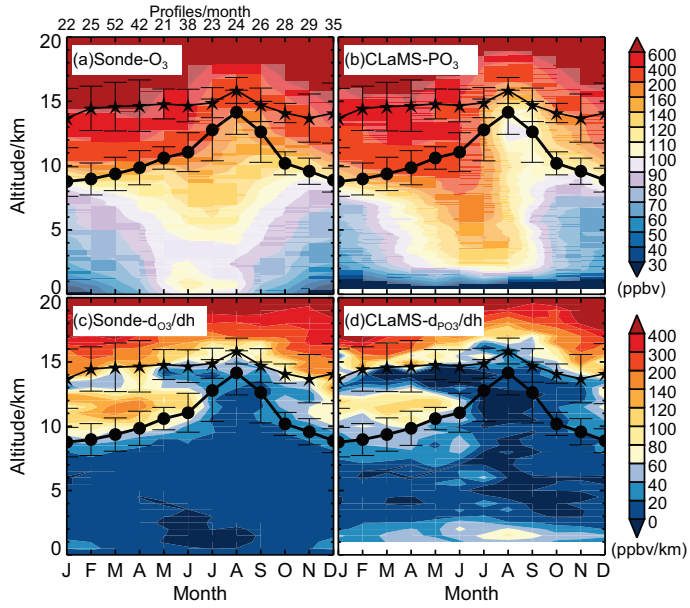

Figure 3.9: The 2002–10 seasonality of ozone over Beijing from (a) ozonesonde observation, (b) CLaMS simulations and the respective vertical gradients (c,d). The first (LRT1) and second (LRT2) thermal tropopause are shown as thick lines with solid dots and stars, respectively (adapted from *Wang et al.* (2012)).

increased industrial and traffic activities in and around Beijing. Following *Wang et al.* (2012), this maximum also explains a clear positive trend for the tropospheric column ozone in the summer maximum over the past decade of around ≈3%/year. However, the question still remains: What is the contribution of the stratospheric ozone both to the observed seasonality and to the inferred trend?

Analysis of the CLaMS simulation with the passively transported ozone, i.e. by switching off of all tropospheric sources and sinks (panel (b) in fig. 3.9), reproduces the observed seasonality well, both in the stratosphere and in the upper troposphere, but not in the lower tropopause between 0 and 2 km. Clearly enhanced O_3 values and a negative O_3 gradient observed during spring and summer in the lower troposphere could not be diagnosed in CLaMS simulations ((c) versus (d) in fig. 3.9). This emphasizes the importance of photochemistry, in particular of the smog chemistry during these seasons. Thus, although transport rather than chemistry drives the seasonality of O_3 around the tropopause, the dynamical processes alone cannot explain the notable trend of lower tropospheric O_3 in the observations.

The last and also the most recent example of how CLaMS simulations have contributed to improving our understanding of the long-term variability of the atmosphere are related to the tropical trends of water vapor in the lower stratosphere. Stratospheric water vapor is a powerful greenhouse gas and important driver of decadal global surface climate change (*Solomon et al.*, 2010; *Dessler et al.*, 2013; *Hegglin et al.*, 2014). Although the stratospheric water vapor entry values roughly follow the evolution of tropical tropopause temperatures, the origin of their multi-timescale variations and possible trends are subject of current scientif c debate (*Fueglistaler and Haynes*, 2005; *Fueglistaler et al.*, 2013; *Urban et al.*, 2014; *Hegglin et al.*, 2014).

The most pronounced signature of water vapor variations in the tropical lower stratosphere is the tape recorder effect (*Mote et al.*, 1996) ref ecting the seasonal cycle of tropical tropopause temperatures. Beyond this annual cycle, the inter-annual variability is mainly inf uenced by the quasi-biennial oscillation (QBO, mean period of 28 to 29 months) (*Baldwin et al.*, 2001; *Dessler et al.*, 2013) and to a weaker extent by the El Nino Southern Oscillation (ENSO) (*Randel et al.*, 2004; *Calvo et al.*, 2010). In addition to these almost periodic components, transient, sub-seasonal cooling episodes occur at timescales of 1-2 months as a result of forcing by extratropical waves (*Randel et al.*, 2002).

In two recent papers, *Tao et al.* (2015a) and *Tao et al.* (2015b) show how the major Sudden Stratospheric Warmings (SSWs) inf uence not only the sub-seasonal variability of water vapor in the lower stratosphere but may also inf uence the long-term trends. Major SSWs are among the most impressive dynamical events in the physical climate system. Driven by the breaking of planetary waves propagating up from the troposphere, these extreme events involve a large and rapid temperature increase (>30-40 K in a matter of days) in the middle to lower stratosphere (30-50 km) and a complete reversal of the climatological westerly zonal-mean wind associated with the stratospheric polar night jet (*Butler et al.*, 2015).

In a case study of a remarkable major SSW in January 2009, *Tao et al.* (2015a) show how a strongly disturbed stratospheric dynamics manifested itself in an accelerated polar descent and tropical upwelling. During the following two weeks up to the end of January, this transient signal of cross-isentropic transport propagated down from around 1 hPa to 100 hPa. The radiative relaxation of this anomaly in diabatic heating was relatively fast (10 days) in the upper stratosphere, but took more than a month in the lower stratosphere, which resulted in accelerated polar descent and accelerated tropical upwelling through late March.

Fig. 3.10 gives an overview of the dynamical background during boreal winter 1998/99 based on ERA-Interim reanalysis. Fig. 3.10a shows that the sudden rise of the polar cap temperature started in the upper stratosphere, around January 10 at 1 hPa, then the warming propagated downward, reaching 10 hPa and descended to the lower stratosphere until late January. The increase of polar temperature was accompanied by the generation of easterlies, which are also shown in f g. 3.10a (black contours).

Before the major SSW, the lower stratosphere in the tropics was slightly warmer than the long-term average due to the westerly phase of the QBO in this winter. Similar to the warming

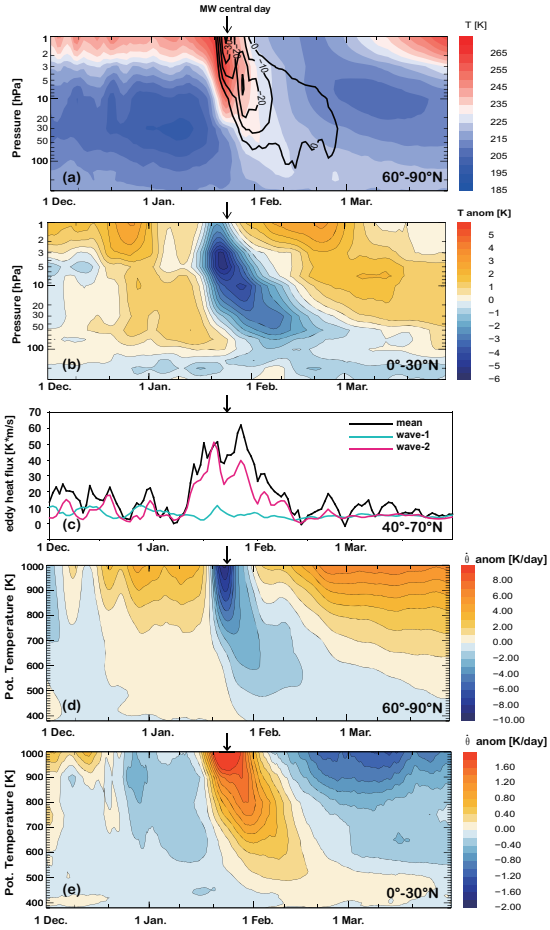

Figure 3.10: (a) Polar cap area weighted mean temperature (60° - 90°N) overlaid with zonal mean easterlies at 60°N (black contours in m/s), (b) tropical zonal mean temperature anomaly from the 24-year climatology (0° - 20°N), (c) eddy heat flux (40° - 70°N, black) on 100 hPa and its decomposition into wave-1 (blue) and wave-2 (red) components (d) polar mean (60° - 90°N) anomaly of the heating rates from the 24-year climatology $Q = d\theta/dt = \dot{\theta}$, (e) same as (d) but for 0° - 30°N. The figures are based on the ERA-interim reanalysis (adapted from *Tao et al.* (2015a)).

in the high latitudes, the tropical cooling (fig. 3.10b) also started around January 15 at 1 hPa and descended from the upper to the lower stratosphere over 2 weeks.

As discussed in *Randel et al.* (2002), time-dependent upwelling in the tropical lower stratosphere is correlated with transient extratropical planetary waves, which transport heat from the tropics to high latitudes and, in turn, drive the BD circulation.

Large-scale tropospheric waves can propagate upward into the stratosphere through weak westerlies and break at the critical level, disturbing the mean flow (*Dickinson*, 1968; *Matsuno*, 1971). Such transient wave breaking converts the zonal flow momentum to mean meridional circulation, and thus drives the extratropical downwelling and tropical upwelling of the BD circulation (e.g., *Holton et al.*, 1995). The temperature perturbations discussed above and shown

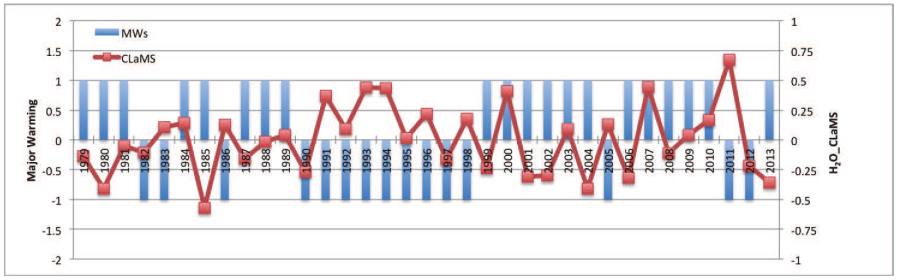

Figure 3.11: The bar chart shows the record of major SSWs from 1979 to 2013: winters with major SSWs are valued 1 and winters without major SSWs are values -1. The scatter-line shows the mean water vapor mixing ratio (400 K, 10°N-10°S, unit: ppmv) of February, March and April using CLaMS simulation (adapted from *Tao et al.* (2015b)).

in f g. 3.10 (a,b) result directly from diabatic heating and cooling caused by these wave-driven vertical motions. Subsequently, temperatures gradually relax toward their radiative equilibrium values by additional radiative cooling or heating, causing vertical motion, i.e. down- or up-welling through isentropic surfaces. The polar and tropical heating rate anomalies from the 24-year mean of ECMWF meteorological ERA-Interim reanalysis (*Dee et al.*, 2011) are shown in f g. 3.10 (d,e). As expected, diabatic polar downwelling and tropical upwelling (quantif ed by these heating rates) were both accelerated after the onset of the major SSW.

In the second related publication, *Tao et al.* (2015b) diagnosed a clear dehydration of air entering the tropical stratosphere after major SSWs. Based on simulations with CLaMS for the 1979-2013 period, driven by the ECMWF ERA-Interim reanalysis, the dehydration effect of major SSWs reaches its maximum about 2-4 weeks after the central date of the major SSW, and strongly depends on the QBO phase. The major SSW-associated drying effect possibly contributes to the long-term variability of stratospheric H_2O (see f g. 3.11) To emphasize this point, we averaged H_2O in the tropical lower stratosphere (400K) from February to April every year and plotted these H_2O values together with the decadal frequency of major SSWs. Fig. 3.11 shows a clear anti-correlation between the major SSW occurrences and H_2O values in the three decades.

4 Relevant publications for this "kumulative Habilitationsschrift"

The following 16 publications (divided into four groups following the outline described in the introduction (section 1.2)) are attached to this "kumulative Habilitationsschrift".

- Asian monsoon and the seasonality of tropical ozone in the lower stratosphere

  1. *Konopka et al.* (2009): Fig. 3.3a in section 3.1

     This paper gave for the f rst time a new explanation of the annual cycle of ozone in the tropical lower stratosphere with a pronounced maximum in late summer and fall due to isentropic in-mixing of extratropical ozone into the tropical lower stratosphere. In this paper, I also connected this effect with the Asian monsoon anticyclone driving this type of transport. J.-U. Grooß provided me with photolytical ozone production rates and satellite-based data (HALOE), which were used for validation of the idealized trajectory model applied in this study. F. Ploeger and R. Müller contributed to discussions during the formulation of the paper.

  2. *Konopka et al.* (2010): Fig. 3.2 in section 3.1

     Here, I discussed the same question as in *Konopka et al.* (2009) but within the framework of our f rst multi-annual CLaMS run. Almost all other co-authors contributed to this simulation: J.-U. Grooß and R. Pommrich designed a simplif ed chemistry, G. Günther designed the water vapor module and helped to organize the necessary computer support. N. Livesey helped to apply the satellite-based data (MLS) for model validation. The other co-authors contributed to the discussions during the formulation of the paper.

  3. *Ploeger et al.* (2012): Fig. 3.3b) in section 3.1

     The main goal of this paper was to f nd out if signatures of in-mixing, i.e. of enhanced isentropic transport from the extra-tropics into the tropical lower stratosphere can also be seen in trace gases like water vapor or CO (i.e. not only in ozone). This paper was strongly motivated be my previous paper on in-mixing and was a next step proving that this effect is relevant for our understanding of the seasonality of transport in the TTL. F. Ploeger, who has been supervised by myself during his PhD study, wrote this paper with my advisory support. C. Manners and P. Forster provided us with the radiation module, T. Schmidt

calculated the climatology of tropical temperature from the GPS radio occultation measurements (CHAMP). Other co-authors helped to design the backward-trajectory calculations and contributed to discussions during the formulation of the paper.

4. *Abalos et al.* (2013): Fig. 3.4) in section 3.1

   This paper was motivated by discussions during the SPARC Workshop on the Brewer-Dobson Circulation in June 2012 where two different views on the explanation of the annual cycle of ozone in the TTL were presented. To reconcile differences in quantifying in-mixing, these two different views, mainly based on the Eulerian methods (M. Abalos and W. Randel) and on the Lagrangian methods (F. Ploeger and myself) were critically compared in this paper. Whereas M. Abalos and F. Ploeger carried out all the calculations, W. Randel and myself contributed to the formulation of the paper.

5. *Konopka et al.* (2015): Fig. 3.1 (middle row) in section 3.1

   The question of understanding the annual cycle of the composition of air in the lower stratosphere was extended in this paper to the analysis of mean age. Using the Transformed Eulerian Mean (TEM) formalism applied to CLaMS simulations and ERA-Interim data, the paper explains the reasons for hemispheric asymmetries and for the annual cycle of age of air observed in MIPAS as well as in *in situ* data. F. Ploeger provided me with all necessary, TEM-based calculations. Other co-authors, especially T. Birner contributed a critical discussion helping to clarify our main statements.

- Mixing-driven origin of the Extratropical Transition Layer (ExTL) and of the Tropopause Inversion Layer (TIL)

  1. *Pan et al.* (2009): Fig. 3.6 (left column) in section 3.2

     In this paper L.L. Pan presented the first, satellite-based (HIRDLS) vertical cross sections of two tropopause folds with strong signatures of stratosphere-troposphere exchange. My contribution was to provide CLaMS-based trajectories discussing the origin of air involved in this mixing event. D. Tarasic provided us with *in situ* ozone profiles for validation of the HIRDLS observations. Other co-authors are members of the HIRDLS satellite group. W. Randel contributed to the formulation of the paper.

  2. *Vogel et al.* (2011): Fig. 3.6 (top right) in section 3.2

     This paper is a result of collaboration between IEK7 at Forschungszentrum Jülich and the Atmospheric Chemistry Division in NCAR (Boulder, USA) where CLaMS was applied for interpretation of *in situ* observations during the Stratosphere-Troposphere Analyses of Regional Transport (START08) campaign. Visiting Boulder several times I prepared all necessary modeling tools to run CLaMS at NCAR during and after the campaign. B. Vogel participated in the campaign and wrote this paper showing how CLaMS can reproduce the observed mixing events both in the 3d physical space as well as in tracer-tracer space where

the observations were available. Together with L.L. Pan I strongly contributed to this novel method of model validation. G. Günther and R. Müller also contributed to the interpretation of the observations. Other co-authors are members of the START08 team who provided us with *in situ* observations, meteorological NCEP data, and satellite observations which were necessary to run CLaMS.

3. *Konopka and Pan* (2012): Fig. 3.7 and 3.6 (bottom right) in section 3.2

   In this paper we developed a new picture of the Extratropical Transition Layer (ExTL) postulating that the isentropic mixing of barotropic (above the jets) and baroclinic (below the jets) Rossby waves are the main mechanism forming ExTL. Here, my part was to use CLaMS and to show how particular observed mixing events are resolved by the model. L.L. Pan was a very good motivator for this work and she also provided me with all necessary observations (mainly tracer-tracer correlations) to validate the model. She also strongly contributed to the formulation of the paper.

4. *Kunz et al.* (2009): Fig. 3.8 in section 3.2

   A. Kunz wrote this paper during her PhD work which was supervised by myself. Using SPURT observations (SPURen-stofftransport in der Tropopausenregion), we have shown in this paper that the formation of the TIL is related to strong mixing events def ning the composition of this layer. The idea for this paper resulted from discussions with W. Randel during my visit in NCAR one year before. R. Müller, L. L. Pan and C. Schiller contributed with their important comments to the f nal version of the paper. F. Rohrer contributed a temporal variance analysis of the original data. The radiation calculations were done using CLaMS radiation module provided by myself.

- Climatological relevance of mixing and interpretation of trends

  1. *Riese et al.* (2012): Fig. 1.2 in section 1.1, see also section 3.3

     This paper was initiated and written by M. Riese. My contribution was related to application of CLaMS in this study, in particular to use of different mixing parameters in order to estimate the impact of mixing on the variability of tracer distributions in the UTLS region. All sensitivity studies with CLaMS were carried out be F. Ploeger and B. Vogel. The radiation calculations to investigate the inf uence of uncertainties in the atmospheric mixing on the uncertainties in radiative forcing were done by A. Rap and P. Forster. M. Dameris contributed with analysis of related uncertainties in transport of water vapor and cloud water in the ECHAM4 GCM and their impact on the cold bias in this GCM.

  2. *Wang et al.* (2012): Fig. 3.9 in section 3.3

     This paper is a f rst published result of collaboration between IEK7 at Forschungszentrum Jülich and Institute of Atmospheric Physics (IAP), Chinese Academy of Sciences in Beijing. This paper was also a part of the PhD work of Y. Wang supervised by myself. During

his one year visit in FZJ, he used the CLaMS model for understanding of the pollution-driven ozone formation over Beijing. The Chinese observations of the ozone trend from 2002 to 2010 were interpreted with CLaMS. The respective model simulations were carried out by F. Ploeger and myself. R. Müller and M. Riese contributed to the formulation of the paper. Y. Wang wrote the paper and the other Chinese co-authors provided us with the ozone sonde observations as well as helped us to calibrate this long time series.

3. *Tao et al.* (2015a): Fig. 3.10 in section 3.3

   This paper written by M. Tao is part of her PhD thesis which was supervised by myself and which will be submitted at the end of 2015. In this paper we combined some previous experiences of M. Tao related to Sudden Stratospheric Warmings with my experience related to modeling of such events with CLaMS. K. A. Walker provided us with satellite data (ACE). The support of J.-U. Grooß was related to model initialization and some trajectory-based sensitivity studies with respect to chemistry. F. Ploeger helped us by comparing model results with MLS observations. R. Müller, C. M. Volk and M. Riese contributed to the formulation of the paper.

4. *Tao et al.* (2015b): Fig. 3.11 in section 3.3

   Similar as above, this paper is also a part of M. Tao's PhD thesis supervised by myself. The idea to this paper is a logical next step in the investigation of the inf uence of Sudden Stratospheric Warmings on the budget of water vapor in the lower tropical stratosphere by extending the results of a case study published in *Tao et al.* (2015a) to a long time series covering several decades. CLaMS simulations extending over the time period from 1979 to 2013 were carried out by F. Ploeger and by myself. Statistical investigations were done by M. Tao. She also wrote this paper. R. Müller, C. M. Volk and M. Riese contributed to the f nal formulation of the paper.

- Development of CLaMS

1. *Ploeger et al.* (2010): see text in section A.1

   This paper was written by F. Ploeger during this part of his PhD time which was supervised by myself. In particular, my contribution was related to implementation of different types of vertical velocities (diabatic and kinematic) into the ClaMS trajectory module. F. Ploeger not only wrote this paper but also used for the f rst time the ERA-Interim product to drive CLaMS model. G. Günther, J.-U. Grooß and and R. Müller contributed to the f nal formulation of the paper.

2. *Ploeger et al.* (2011): Fig. A.1 and A.2 in section A.1

   Also this paper is part of F. Ploeger's PhD work and is the natural continuation of results obtained in *Ploeger et al.* (2010). Here experimental data were included in order to decide which vertical velocities, diabatic or kinematic, give a better description of transport in

the UTLS region. The experimental data were provided by F. Ravegnani, C. Schiller and A. Ulanovski. My contribution was to design numerical experiments reconstructing the observations by using back-trajectories. J.-U. Grooß and G. Günther helped to develop appropriate chemistry and cirrus modules. S. Fueglistaler, Y.S. Liu, R. Müller and M. Riese contributed to the final formulation of the paper.

3. *Konopka et al.* (2012): all figures in section 2.5

   This paper describes how to define in a physical way the irregular CLaMS grid. This method is used in the current version of the model. F. Ploeger and R. Müller helped to develop these ideas as well as to formulate the paper.

A Appendix

A.1 Vertical velocity

Usually two types of vertical velocities w are used for modeling of the atmospheric transport, referred to as "diabatic" and "kinematic" (*Eluszkiewicz et al.*, 2000; *Schoeberl et al.*, 2003). "Diabatic" denotes transport calculations in an isentropic coordinate system θ with cross-isentropic motion $\dot{\theta} = D\theta/Dt$ determined from diabatic heating rates J due to radiation, latent heat and other diabatic processes, e.g. due to shear-f ow turbulent mixing (e.g. *Andrews et al.*, 1987; *Flannaghan and Fueglistaler*, 2011), i.e.:

$$c_p \frac{D\theta}{Dt} = J \frac{\theta}{T} \,. \tag{A.1}$$

Here T and c_p denote the temperature f eld and the specif c heat at constant pressure p, respectively ($c_p \approx 1006$ J/(kg K) for dry air).

On the other hand "kinematic" stands for transport across pressure surfaces p with the pressure tendency $\dot{p} = Dp/Dt = \omega$ as the vertical velocity. ω is derived from eq. (2.13), i.e. by vertically integrating the continuity equation from surface pressure p_s to p (e.g., *Holton*, 1992, Chapt. 3.5):

$$\omega = \omega_s - \int_{p_s}^{p} \nabla_h \cdot (u, v)\, \mathrm{d}p \,, \qquad \nabla_h = (\partial_x, \partial_y) \,. \tag{A.2}$$

Commonly, the hydrostatic approximation is assumed, i.e. the vertical balance of momentum reduces to $\partial_z p = \rho g z$. Thus, the continuity equation (2.13) rather than the vertical balance equation has to be used to derive ω. An obvious advantage of the ω-wind is the fact that, in contrast to the diabatic approach, the condition of the divergence-free velocity f eld is fulf lled per def nition and, consequently, the air mass density ρ is conserved. Because the diabatic vertical velocities are not mass conserving per se, the horizontal winds have to be corrected in such a way that the divergence of the 3D velocity vector vanishes (*Wohltmann and Rex*, 2008).

However, the nearly adiabatic nature of the atmospheric large-scale motion, with the f ow mainly being along surfaces of constant potential temperature, seems to favor the diabatic approach based on the isentropic coordinate system (*Mahowald et al.*, 2002). On the other hand, the ω-wind is calculated as a small residual between the large horizontal wind terms in eq. (A.2). Such vertical velocity is strongly disturbed by atmospheric waves, like planetary or gravity waves, which are mostly adiabatic processes.

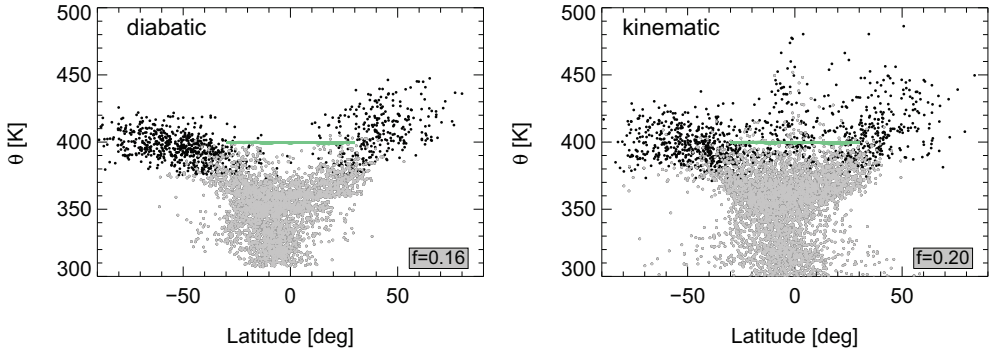

Figure A.1: Vertical dispersion of backward trajectories, starting at 400 K, in the latitude/potential temperature plane after 45 days of backward integration during winter (on the northern hemisphere). The green horizontal bar displays the initialization locations. Left/Right: Position of the trajectories driven by the diabatic/kinematic ECMWF velocities (adopted from *Ploeger et al.* (2011)).

Thus, by using θ rather than p as vertical coordinate, the adiabatic oscillations of air masses do not influence the calculation of the vertical velocity and, consequently, only diabatic processes directly drive the (cross-isentropic) advection (compare eq. (A.1)). Furthermore, the kinematic approach is not only an "ill-conditioned" problem but is also disturbed by the deficiencies of the assimilation procedures (*Eluszkiewicz et al.*, 2000; *Schoeberl et al.*, 2003; *Konopka et al.*, 2007; *Wohltmann and Rex*, 2008; *Ploeger et al.*, 2010).

An example of the differences between trajectory calculations driven by the diabatic and kinematic velocities as provided by the ECMWF meteorological fields is shown in fig. A.1. Here, the vertical dispersion of the backward trajectories in the latitude/potential temperature space is shown after 45 days of integration. The trajectories were started at $\theta = 400$ K (green horizontal bar). The diabatic scenario (right) shows an expected behavior of the air parcel distribution with the majority of air parcels ascending from below through the lower and mid tropics. On the contrary, the kinematic approach leads to much higher vertical dispersion. The "Ψ shape" of the distribution in the kinematic scenario is due to nonphysical subsidence of the air parcels above the tropical tropopause and indicates, in agreement with (*Schoeberl et al.*, 2003), significant deficiencies of the kinematic velocities (*Ploeger et al.*, 2010, 2011).

This fact could also be confirmed by a comparison of reconstructed ozone profiles with in situ observations (see fig. A.2). Here, a better agreement of the diabatic (red) versus kinematic (black) approach with the observed profiles (gray) is another aspect in favor of the $\dot{\theta}$-related vertical velocities (*Ploeger et al.*, 2011).

Last but not least, in contrast to the (prognostic) kinematic view, the (diagnostic) diabatic approach allows to distinguish between different physical processes, which are responsible for the vertical motion. In particular, contributions of clear sky radiation, radiative effects of clouds,

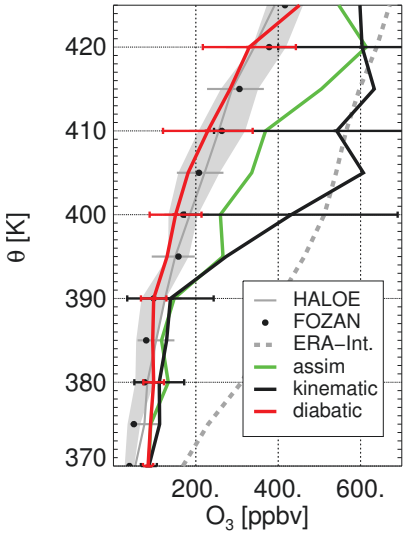

Figure A.2: Mean ozone profiles during the SCOUT-O3 campaign, in 5K potential temperature bins. In situ observations are from the FOZAN instrument (black dots, gray range 1-standard deviation). Gray solid lines (bars show 1-standard deviation) are HALOE measurements. Predictions based on kinematic (black) and diabatic (red) trajectories are shown as solid lines. The thick dashed gray line denotes ozone from ERA-Interim data (adapted from *Ploeger et al.* (2011)).

latent heat and other diabatic processes such as turbulent diffusion can be separated from each other.

A.2 Effective horizontal diffusivity

The idea of the effective diffusivity is to parameterize both the diffusive and advective parts of transport which occur on unresolved scales of the model by using an appropriate diffusion coeff cient. In the atmosphere, which is dominated by horizontal motion, this can be done in terms of only one effective horizontal diffusion coeff cient.

Thus, we assume that horizontal rather than vertical wind dominates the unresolved scales of the atmosphere and that the spatial variability of the wind can be characterized by some typical values of the vertical shear and horizontal strain, i.e. $s_v \approx 10^{-3}$ s^{-1} and $s_h \approx 10^{-5}$, respectively (*Dürbeck and Gerz*, 1995; *Balluch and Haynes*, 1997). Furthermore, we assume that the varying horizontal wind uniformly covers all possible directions and that the vertical and horizontal diffusivities on the (unresolved) scales are quantif ed by the respective coeff cients D_v^0 and D_h^0 (see f g. A.3).

Let us now release a Gaussian plume, with an initial spherical symmetry and with a geometric extension being below the considered unresolved spatial scales. During the dispersion, the vertical wind shear elongates such a plume whereas the diffusion works against such elongation. For a constant wind direction, similar behavior is expected on the horizontal scale although with a much smaller elongation due to $s_h \ll s_v$. Using coordinates moving with the plume (Lagrangian frame of reference), the solution of the corresponding diffusion equation is a Gaussian

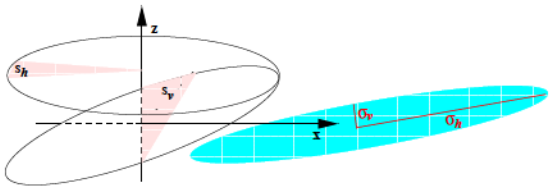

Figure A.3: Plume dispersion driven by unresolved horizontal wind (in x-y plane) with typical vertical and horizontal shear rates s_v and s_h, respectively and a uniform contribution of all horizontal directions of the wind. In particular, the elongation of the 2D plume (in x-z plane) is shown, which results in a slanted blue ellipse with the horizontal and vertical variances given by σ_h and σ_v.

distribution (*Konopka*, 1995) that can be transformed to the principal axes.

Thus, for a 2D case with a prescribed wind along the x axis, the 2D plume in the x-z plane is elongated by the vertical shear s_v and by the diffusivities D_h^0 and D_v^0 into an almost horizontal ellipse with the horizontal and vertical variances σ_h and σ_v, respectively (blue ellipse in f g. A.3). In the 3D case and after a suff ciently long time during which we assume that the horizontal wind has uniformly covered all possible directions, a symmetric (around the z-axes), pancake-like Gaussian cloud is expected. This rotation-symmetric distribution can be expressed in terms of only two variances σ_h and σ_v with $\sigma_h \gg \sigma_v$ because $s_h \ll s_v$ and $D_h^0 \gg D_v^0$ is valid (more precisely, σ_h and σ_v are the diagonal elements of the rotation-symmetric variance matrix describing the 3D width of the Gaussian cloud). The time evolution of σ_h and σ_v is given by:

$$\frac{d\sigma_h}{dt} = -s_h\sigma_h + D_h^0 \tag{A.3}$$

$$\frac{d\sigma_v}{dt} = -s_v\sigma_v + D_v^0 \tag{A.4}$$

In a steady state, i.e., when effects of advection and diffusion cancel each other, the left sides of the above equations vanish, i.e. the following is obtained:

$$\alpha^2 \approx \frac{\sigma_h}{\sigma_v} = \frac{s_v}{s_h}\frac{D_h^0}{D_v^0} =: \frac{D_h}{D_v} \tag{A.5}$$

with the horizontal effective diffusivity $D_h = (s_v/s_h)D_h^0$ quantifying the advective and diffusive contributions of the unresolved scales. Furthermore, with $D_v = D_v^0$, we assume that the vertical diffusivity is roughly the same on the resolved and unresolved vertical scale.

The ratio of the vertical and horizontal shear rates, s_v/s_h can be approximated through $s_v/s_h \approx 10^{-3}/10^{-5} = 100$ (*Dürbeck and Gerz*, 1995; *Balluch and Haynes*, 1997), and D_h^0 is a small-scale, horizontal diffusivity with $D_h^0 \approx 10$ m^2/s (*Schumann et al.*, 1995) (D_h^0 can be interpreted as a horizontal diffusivity in a wind-free atmosphere valid on horizontal scales within the range $1 - 100$ m). Thus, using these numbers, D_h is expected to be of the order of 10^3 m^2/s.

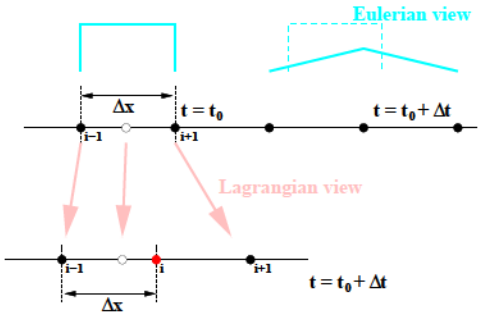

Figure A.4: Idealized 1D transport in the Eulerian (blue) and Lagrangian (orange) frame of reference. The error of interpolation can be re-interpreted as the numerical diffusion (for details see text).

A.3 Interpolation and numerical diffusion

In this appendix, we show that in a 1-D transport problem, both from the Lagrangian and Eulerian point of view, the error connected with the re-gridding and associated interpolation can be understood as a numerical diffusion with a constant diffusivity $D \sim \Delta x^2/\Delta t$, where Δx and Δt describe the grid width and the integration time step.

Let us first consider the Lagrangian case, i.e. two air parcels separated by the distance Δx (points $i-1$ and $i+1$ in fig. A.4), which after a time step Δt move so far apart that an additional air parcel has to be inserted in-between (red point i). Thus, the mixing ratio μ_i of a passive tracer at the point i can only be derived from μ_{i-1} and μ_{i+1}, which are the mixing ratios of the next neighbors of the air parcel i. The easiest form of interpolation, i.e. linear interpolation, gives:

$$\mu_i^{\Delta t} = \frac{1}{2}(\mu_{i-1}^{\Delta t} + \mu_{i+1}^{\Delta t}) = \frac{1}{2}(\mu_{i-1} + \mu_{i+1}) \tag{A.6}$$

because μ_{i-1} and μ_{i+1} are transported along the trajectories without changing their values (beige arrows).

However, in this way an error has crept into the numerical scheme, because $\mu_i^{\Delta t}$ deviates from μ_i describing the "true" mixing ratio at the i-th air parcel. The origin of this error becomes also apparent in the fact that the middle point between the air parcels $i-1$ and $i+1$ at $t = t_0$ (open circle) is not transported to the position of the i-th air parcel at $t = t_0 + \Delta t$ (red filled circle). Thus, even if μ_i at the middle point between the air parcels $i-1$ and $i+1$ at $t = t_0$ were known, this would not help to determine the "true" value $\mu_i^{\Delta t}$ at the red point (anyway, this information falls below the resolution Δx and, consequently, is not available).

The error of interpolation can be estimated as $\mu_i^{\Delta t} - \mu_i$, i.e.:

$$\mu_i^{\Delta t} - \mu_i = \frac{1}{2}(\mu_{i-1} - 2\mu_i + \mu_{i+1}) \tag{A.7}$$

or

$$\frac{\mu_i^{\Delta t} - \mu_i}{\Delta t} = \frac{1}{2}\frac{\mu_{i-1} - 2\mu_i + \mu_{i+1}}{\Delta x^2}\frac{\Delta x^2}{\Delta t}\,. \tag{A.8}$$

The last equation is a discretized form of the diffusion equation $\partial_t \mu = D\partial_x^2 \mu$ with a constant diffusivity $D = 0.5\Delta x^2/\Delta t$ (forward difference quotient in time), i.e. from this equation $\mu_i^{\Delta t}$ can be derived if the values μ_{i-1}, μ_i and μ_{i+1} are known.

Thus, because the original Lagrangian transport problem was traced back to a simple diffusion equation, the interpolation error in a Lagrangian transport scheme (from the upper to the lower line in f g. A.4) can be reinterpreted as a numerical diffusion with the diffusivity given by $D \sim \Delta x^2/\Delta t$. Similarly, in the Eulerian frame of reference, the interpolation of the advected tracer on the background grid smoothes out the mixing ratio distribution in the same way as if diffusivity were active. In particular, an advected rectangle (solid to dashed cyan rectangle along the upper line f g. A.4) becomes, by re-sampling on the background grid, a triangle. Using the same arguments as above, the discretized form of the diffusion equation with $D \sim \Delta x^2/\Delta t$ can be derived that mimics the tracer transport affected by such interpolations. Note that with Δt and Δx becoming smaller, the interpolation error and the numerical diffusion go to zero. Furthermore, the interpolation type (e.g. linear or logarithmic) inf uences the numerical value of the numerical diffusivity.

A.4 Idealized 2D f ows

To illustrate and also to explain most of the proposed concepts of deformation-driven mixing, it is convenient to use some idealized 2D f ows such as pure shear, strain and rotation f ows which can be def ned using a linear operator $\mathbf{A}$, i.e.

$$\mathbf{u} = \mathbf{A} \cdot \mathbf{r}, \qquad \mathbf{u} = (u, v), \quad \mathbf{r} = (x, y) \tag{A.9}$$

with $\mathbf{A}$ given as the following 2×2 matrices:

$$\mathbf{R} = \frac{s}{2}\begin{pmatrix} 0 & 1 \\ -1 & 0 \end{pmatrix}, \quad \text{pure rotation} \tag{A.10}$$

$$\mathbf{S}_t = \frac{s}{2}\begin{pmatrix} 0 & 1 \\ 1 & 0 \end{pmatrix}, \quad \text{pure strain} \tag{A.11}$$

$$\mathbf{S}_h = s\begin{pmatrix} 0 & 1 \\ 0 & 0 \end{pmatrix}, \quad \text{pure shear.} \tag{A.12}$$

For all 3 operators, s denotes the rotation, strain and shear rate. Note that all 3 types of f ow are divergence-free (i.e. $\partial_x u + \partial_y v = 0$) and that the relation $\mathbf{S}_h = \mathbf{R} + \mathbf{S}_t$ is valid (f g. A.5).

Using these idealized f ows the trajectory equation:

$$\frac{d\mathbf{r}(t)}{dt} = \mathbf{u}(\mathbf{r}(t), t), \quad \mathbf{r}(0) = \mathbf{r}_0 \tag{A.13}$$

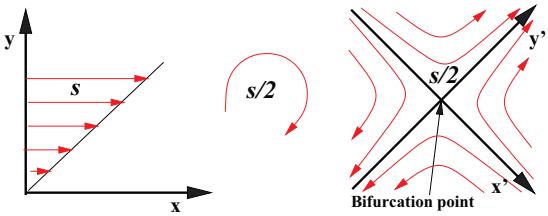

Figure A.5: Idealized 2D flows. Pure shear flow $\mathbf{S}_h$ with the shear rate s can be formally decomposed into pure rotation $\mathbf{R}$ with the rotation rate $s/2$ and pure strain $\mathbf{S}_t$ with the strain rate $s/2$. In the bifurcation point ($x' = y' = 0$) the trajectories behave in a highly non-linear manner, i.e. a small displacement completely changes the direction of the trajectory (*Bowman et al.*, 2007).

can be explicitly solved owing to the linearity of $\mathbf{u}$ with respect to $\mathbf{r}$ (*Perko*, 1996). After some reformulation we get:

$$\mathbf{r}(s,t,\mathbf{r_0}) = \mathbf{F}(s,t)\cdot\mathbf{r_0} \tag{A.14}$$

with the matrix $\mathbf{F}$ given as

$$\mathbf{F}_R = \begin{pmatrix} \cos\phi & \sin\phi \\ -sin\phi & \cos\phi \end{pmatrix}, \quad \phi = \frac{st}{2} \tag{A.15}$$

$$\begin{aligned} \mathbf{F}_{S_t} &= \frac{1}{2}\begin{pmatrix} 1 & 1 \\ 1 & -1 \end{pmatrix}\begin{pmatrix} \gamma_+ & 0 \\ 0 & \gamma_- \end{pmatrix}\begin{pmatrix} 1 & 1 \\ 1 & -1 \end{pmatrix} = \\ &= \frac{1}{2}\begin{pmatrix} \gamma_+ + \gamma_- & \gamma_+ - \gamma_- \\ \gamma_+ - \gamma_- & \gamma_+ + \gamma_- \end{pmatrix}, \gamma_\pm = \exp\frac{\pm st}{2} \end{aligned} \tag{A.16}$$

$$\mathbf{F}_{S_h} = \begin{pmatrix} 1 & st \\ 0 & 1 \end{pmatrix} \tag{A.17}$$

for rotation, strain and shear deformations, respectively. Note that despite the decomposition property $\mathbf{S}_h = \mathbf{R} + \mathbf{S}_t$, the relation $\mathbf{F}_{S_h} = \mathbf{F}_R \cdot \mathbf{F}_{S_t}$ is not valid. Furthermore, both strain and shear with the same deformation rate s deform a circle into an ellipse with the area of the original circle unchanged although the major and minor axes of the ellipse are different for both deformations. Conversely, for each strain value s a shear s' can be found, that, up to a rotation, deforms a circle into the same ellipse. In addition, for small values of s, the numerical values of s and s' are almost the same.

A.5 Lyapunov exponents

The Lyapunov exponents are commonly used to characterizes the rate of separation of infinitesimally close trajectories (see e.g. *Pierrehumbert and Yang*, 1993; *Ott*, 1993; *Geist et al.*, 1990; *Kantz and Schreiber*, 2004) (see fig. A.6). More precisely, let us consider the solution of the trajectory equation (2.16) for a given velocity field $\mathbf{u}$, i.e. :

$$\mathbf{r}(t) = \mathbf{F}(\mathbf{r_0}, t) \tag{A.18}$$

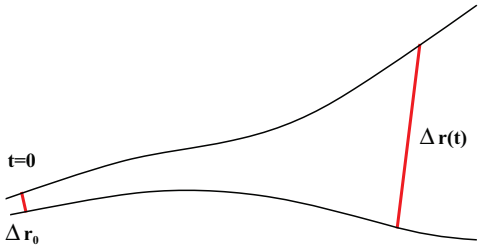

Figure A.6: Two trajectories with initial separation Δr_0 diverge at a rate given by $\Delta r(t) \approx \Delta r_0 \exp(\lambda t)$. λ denotes the Lyapunov exponent.

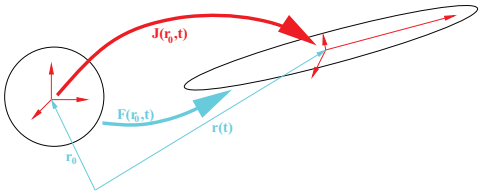

Figure A.7: Deformation along a trajectory $\mathbf{r}(t) = \mathbf{F}(\mathbf{r_0}, t)$ (cyan). The related transformation connecting the tangent spaces at $\mathbf{r_0}$ and at $\mathbf{r}(t)$ is given by the Jacobian $\mathbf{J} = \partial\mathbf{F}/\partial\mathbf{r_0}$ (red). To measure the strength of the related deformation, a symmetric and positively def nite metric is necessary. Its eigenvalues def ne the Lyapunov exponents.

Thus, the Jacobian $\mathbf{J} = \partial\mathbf{F}/\partial\mathbf{r_0}$ describes the linear transformation between tangent spaces at $\mathbf{r_0}$ and at $\mathbf{r}(t)$ (see f g. A.7). The separation rate of the adjacent trajectories can be quantif ed by the strength of the deformation that elongates or shrinks the basis vectors spanning the tangents space at $\mathbf{r_0}$. Commonly, the symmetric and positive def nite second-order tensor (metric) $\mathbf{g}(\mathbf{r_0}, t)$ def ned as

$$\mathbf{g} = \mathbf{J}^T\mathbf{J}, \tag{A.19}$$

is used. Owing to its symmetry, $\mathbf{g}$ is invariant with respect to any rotation and, consequently, can be diagonalized. Because $\mathbf{g}$ is also positively def nite, three positive eigenvalues Λ_i, $i = 1, \ldots, 3$ exist. The time-independent Lyapunov exponents λ_i are then commonly def ned by carrying out an appropriate limes $t \to \infty$, i.e.:

$$\lambda_i = \lim_{t\to\infty} \frac{1}{t} f(\Lambda_i), \quad i = 1, \ldots, 3 \tag{A.20}$$

where f is a strictly monotonically increasing function.

For a pure 2D strain f ow (see eq. (A.16)), the Jacobian is given by $\mathbf{J} = \mathbf{F}_{S_t}$ and, after some easy algebra, the metric and the f nite-time Lyapunov exponents can be written as

$$\mathbf{g}_{st} = \begin{pmatrix} \Lambda_1^{st} & 0 \\ 0 & \Lambda_2^{st} \end{pmatrix}, \quad \Lambda_{1/2}^{st} = \exp \pm st. \tag{A.21}$$

Thus, the time-independent Lyapunov exponents in a pure strain f ow are given by

$$\lambda_{1/2}^{st} = \lim_{t\to\infty} \frac{1}{t} \ln(\Lambda_{1/2}^{st}) = \pm s. \tag{A.22}$$

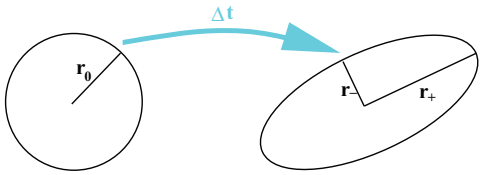

Figure A.8: Lyapunov exponent in a 2D incompressible f ow

Trivially, the Lyapunov exponents for a pure rotational f ow vanish. For a pure 2D shear f ow, metric $\mathbf{g}_{sh}$ can be directly derived from eq. (A.17) as

$$\mathbf{g}_{sh} = \begin{pmatrix} 1 & st \\ st & s^2t^2 \end{pmatrix}. \tag{A.23}$$

Consequently, the f nite-time Lyapunov exponents, i.e. the eigenvalues of $\mathbf{g}_{sh}$, are given by

$$\Lambda^{sh}_{1/2} = \frac{s^2t^2}{2}\left[1 \pm \left(1 + \frac{4}{s^2t^2}\right)^{1/2}\right]. \tag{A.24}$$

For the time-independent Lyapunov exponents we obtain

$$\lambda^{sh}_{1/2} = \lim_{t\to\infty} \frac{1}{t}\sqrt{(\Lambda^{sh}_{1/2})} \tag{A.25}$$

and, consequently, $\lambda^{sh}_1 = s$ and $\lambda^{sh}_2 = 0$. Finally, the def nition of the Lyapunov exponents in an arbitrary 2D incompressible f ow reduces to only one parameter λ (see f g. A.8). This is because in such a f ow a circle with a radius r_0 is transformed during an inf nitesimal time step Δt into an ellipse ($r_\pm$ are the major and minor axes, respectively) with the same area as the original circle (due to incompressibility), i.e. $r_0^2 = r_+ r_-$. The major and minor axes can also be replaced by $r_\pm = r_0 \exp \pm\lambda\Delta t$ where λ is the f nite-time Lyapunov exponent given by:

$$\lambda = \frac{1}{\Delta t}\ln\frac{r_+}{r_0} = \frac{1}{\Delta t}\ln\frac{r_0}{r_-} \tag{A.26}$$

In the limes $t \to \infty$, eq. (A.26) def nes the time-independent Lyapunov exponent.

A.6 Next neighbors, Delaunay triangulation and Voronoi polygons

The handling of irregular grids, especially the determination of the next neighbors in such grids, requires specif c mathematics that will be compiled in this appendix.

The most intuitive def nition of the next neighbors for a given point in an irregular k-dimensional grid can be achieved by using the concept of the Voronoi region (or Voronoi polygon in 2D) def ned as the area where every point is closer to the considered point than to any other grid point

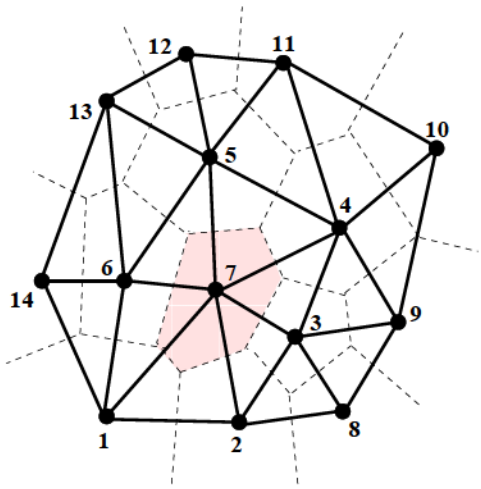

Figure A.9: Voronoi polygons (dashed lines) and Delaunay triangulation (bold lines) def ning the next neighbors in a 2D grid (bold f lled circles).

(see f g. A.9 where beige dashed region denotes the Voronoi region of the point with the number 7 surrounded by the next neighbors numbered from 1 to 6).

The borders of the Voronoi regions are called Voronoi edges (dashed lines) and are the set of points of equal distance to two nearest grid points. The Voronoi edges are symmetry axes for next neighbor grid point pairs. Every grid point lies within exactly one associated Voronoi region. Two grid points which are next neighbors are connected by a Delaunay edge which in the 2D case form a net of triangles, the Delaunay triangulation or, in 3D, the Delaunay tetrahedration. For a comprehensive discussion of all relevant geometric properties of the Delaunay triangulation see Wikipedia and references therein.

To determine the Delaunay triangulation for an arbitrary irregular grid in k-dimensions is a challenging numerical problem. One of the strategies, the convex hull approach is based on the idea that the f nding of the Delaunay triangulation for a set of points in k-dimensional Euclidean space can be converted to the problem of f nding the convex hull for a set of points in $(n+1)$-dimensional space (e.g., *Preparata and Shamos*, 1985).

The convex hull of a set of points X in the Euclidean space is the smallest set that contains X. For a planar set of points, the convex hull may be easily visualized by imagining an elastic band stretched open to encompass these points; when released, it will assume the shape of the required convex hull (see f g. A.10). Fig. A.11 shows schematically for a 1D case how the convex hull strategy works. Thus, f rst the 1D irregular grid points (black f lled circles on the horizontal line) are projected onto the circle arch (2D space). Then the convex hull is iteratively determined ($i = 1$ to 4) where new points are gradually added to the polygonal chain (from blue through green and pink to cyan) until the convex hull is found that, in this simple case, is given by the minimal set containing all the points on the circle.

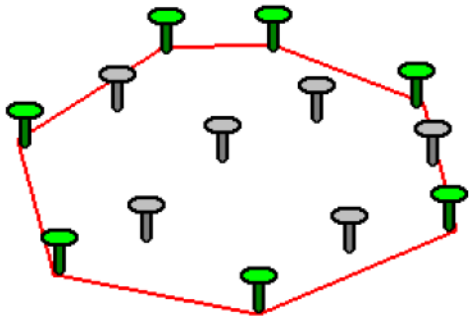

Figure A.10: When X is a set of points on the plane (like nails), the convex hull may be visualized as the shape formed by a rubber band stretched around X. The green nails define the edge of the convex hull whereas the gray nails belong to the interior of the convex hull of X (see Wikipedia).

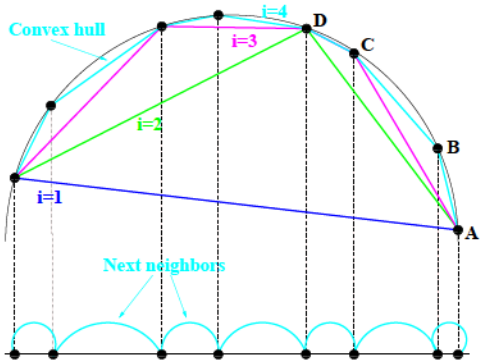

Figure A.11: Strategy of the convex hull algorithm to find the next neighbors in the 1D case.

Thus, after each iteration step i a new point is added to the existing polygonal chain that is outside the chain, i.e. outside the i-th iteration of the convex hull. Only those parts of the chain are modified which "are seen" from the perspective of the new point. For example, during the 4th step point B sees only the points A and C but not the point D. This criterion can also be formalized by using the scalar product between the normal vectors. The iteration is finished if all points are processed and the convex hull (cyan) is found.

Finally, the edges of the convex hull are projected back to the 1D space defining the Delaunay triangulation that reduces in this 1D case to a set of lines. This set also defines the next neighbors of the original grid points (cyan arches).

The 2D/3D cases are natural generalizations of this procedure with triangles and tetrahedra replacing the straight lines as the basic units of the convex hull. In particular, in the 2D case the circle arch in fig. A.11 has to be replaced by a hemisphere and the convex hull is formed by a set of triangles defining the Delaunay triangulation. In this paper, only the case with a co-spherical grid is relevant, i.e. when all grid points which have to be triangulated are on a sphere. The computational times, $t_{2D/3D}$ are of the order $\sim N \log N$ and better than N^2 for the 2D and 3D triangulation, respectively, with N denoting the total number of grid points (*Barber et al.*, 1996).

Bibliography

Abalos, M., F. Ploeger, P. Konopka, W. J. Randel, and E. Serrano (2013), Ozone seasonality above the tropical tropopause: reconciling the eulerian and lagrangian perspectives of transport processes, *Atmos. Chem. Phys.*, *13*(21), 10,787–10,794, doi:10.5194/acp-13-10787-2013, warning: BibtexKey has changed!!

Andrews, D. G., J. R. Holton, and C. B. Leovy (1987), *Middle Atmosphere Dynamics*, 489 pp., Academic Press, San Diego, USA.

Baldwin, M., et al. (2001), The quasi-biennial oscillation, *Rev. Geophys.*, *39*(2), 179–229.

Balluch, M. G., and P. H. Haynes (1997), Quantif cation of lower stratospheric mixing processes using aircraft data, *J. Geophys. Res.*, *102*, 23,487–23,504.

Barber, C. B., P. D. David, and H. Huhdanpaa (1996), The quickhull algorithm for convex hulls, *ACM Transactions on Mathematical Software*, *22*, 469–483.

Batchelor, G. K. (1953), *The Theory of Homogeneous Turbulence*, Cambridge Science Classics, New York.

Birner, T. (2006), Fine-scale structure of the extratropical tropopause region, *J. Geophys. Res.*, *111*(D04104), D04104, doi:10.1029/2005JD006301, warning: BibtexKey has changed!!

Birner, T. (2010), Residual circulation and tropopause structure, *J. Atmos. Sci.*, *67*, 2582–2600.

Birner, T., A. Dörnbrack, and U. Schumann (2002), How sharp is the tropopause at midlatitudes?, *Geophys. Res. Lett.*, *29*(14).

Bowman, K. P., L. L. Pan, T. Campos, and R. S. Gao (2007), Observations of f ne-scale transport structure in the upper troposphere from the High-performance Instrument Airborne Platform for Environmental Research, *J. Geophys. Res.*, *112*(D18111), doi:10.1029/2007JD008685.

Brewer, A. W. (1949), Evidence for a world circulation provided by the measurements of helium and water vapour distribution in the stratosphere, *Q. J. R. Meteorol. Soc.*, *75*(326), 351–363, doi:10.1002/qj.49707532603.

Butler, A. H., D. J. Seidel, S. C. Hardiman, N. Butchart, T. Birner, and A. Match (2015), Def ning sudden stratospheric warmings, *Bulletin of the American Meteorological Society*, doi:0.1175/BAMS-D-13-00173.1.

Calvo, N., R. R. Garcia, W. J. Randel, and D. Marsh (2010), Dynamical mechanism for the increase in tropical upwelling in the lowermost tropical stratosphere during warm ENSO events, *J. Atmos. Sci.*, *67*(7), 2331–2340, doi:10.1175/2010JAS3433.1.

Courant, R., K. Friedrichs, and H. Lewy (1928), Über die partiellen Differenzengleichungen der mathematischen Physik, *Mathematische Annalen*, *100*, 32–74.

Dee, D. P., et al. (2011), The ERA-Interim reanalysis: conf guration and performance of the data assimilation system, *Q. J. R. Meteorol. Soc.*, *137*, 553–597, doi:10.1002/qj.828.

Dessler, A., M. Schoeberl, T. Wang, S. Davis, and K. Rosenlof (2013), Stratospheric water vapor feedback, *Proceedings of the National Academy of Sciences*, *110*(45), 18,087–18,091, doi: 10.1073/pnas.1310344110.

Dethof, A., A. O'Neill, J. M. Slingo, and H. G. J. Smit (1999), A mechanism for moistening the lower stratosphere involving the Asian summer monsoon, *Q. J. R. Meteorol. Soc.*, *556*(125), 1079–1106.

Dickinson, R. E. (1968), On the exact and approximate linear theory of vertically propagating planetary rossby waves forced at a spherical lower boundary, *Monthly Weather Review*, *96*(7), 405–415.

Dürbeck, T., and T. Gerz (1995), Large-eddy simulation of aircraft exhaust plumes in the free atmosphere: Effective diffusivities and cross-sections, *Geophys. Res. Lett.*, *22*, 3203–3206.

Eluszkiewicz, J., R. Hemler, J. Mahlman, L. Bruhwiler, and L. Takacs (2000), Sensitivity of age-of-air calculations to the choice of advection scheme, *J. Atmos. Sci.*, *57*(19), 3185–3201.

Fick, A. (1855), über Diffusion, *Poggendorf's Annalen*, *94*, 59–81.

Flannaghan, T. J., and S. Fueglistaler (2011), On the relationship between the strength of the Brower-Dobson circulation and the age of stratospheric air, *grl*, *38*, doi: 10.1029/2011GL045524.

Folkins, I., P. Bernath, C. Boone, G. Lesins, N. Livesey, A. M. Thompson, K. Walter, and J. C. Witte (2006), Seasonal cycles of O_3, co, and convective outf ow at the tropical tropopause, *Geophys. Res. Lett.*, *33*, L16802, doi:10.1029/2006GL026602.

Fueglistaler, S., and P. H. Haynes (2005), Control of interannual and longer-term variability of stratospheric water vapor, *J. Geophys. Res.*, *110*(D24), D24108, doi:10.1029/2005JD006019.

Fueglistaler, S., H. Wernli, and T. Peter (2004), Tropical troposphere-to-stratosphere transport inferred from trajectory calculations, *J. Geophys. Res.*, *109*(D3), D03108, doi: 10.1029/2003JD004069.

Fueglistaler, S., A. E. Dessler, T. J. Dunkerton, I. Folkins, Q. Fu, and P. W. Mote (2009), Tropical tropopause layer, *Rev. Geophys.*, *47*, RG1004, doi:10.1029/2008RG000267.

Fueglistaler, S., et al. (2013), The relation between atmospheric humidity and temperature trends for stratospheric water, *J. Geophys. Res.*, *118*(2), 1052–1074, doi:10.1002/jgrd.50157.

Garcia, R. R., D. R. Marsh, D. E. Kinnison, B. A. Boville, and F. Sassi (2007), Simulation of secular trends in the middle atmosphere, 1950–2003, *J. Geophys. Res.*, *112*, D09301, doi: 10.1029/2006JD007485.

Geist, K., U. Parlitz, and W. Lauterborn (1990), Comparison of different methods for computing lyapunov exponents, *Prog Theor Phys*, *83*, 875–893.

Gettelman, A., P. Hoor, L. L. Pan, W. J. Randel, M. I. Hegglin, and T. Birner (2011), The extratropical upper troposphere and lower stratosphere, *Rev. Geophys.*, *49*(RG3003), RG3003, doi:10.1029/2011RG000355.

Hall, T. M., and R. A. Plumb (1994), Age as a diagnostic of stratospheric transport, *J. Geophys. Res.*, *99*(D1), 1059–1070.

Haynes, P., and J. Anglade (1997), The vertical scale cascade in atmospheric tracers due to large-scale differential advection, *J. Atmos. Sci.*, *54*, 1121–1136.

Haynes, P., and E. Shuckburgh (2000a), Effective diffusivity as a diagnostic of atmospheric transport, 1, Stratosphere, *J. Geophys. Res.*, *105*, 22,777–22,794.

Haynes, P., and E. Shuckburgh (2000b), Effective diffusivity as a diagnostic of atmospheric transport, 2, Troposphere and lower stratosphere, *J. Geophys. Res.*, *105*, 22,795–22,810.

Hegglin, M. I., et al. (2014), Vertical structure of stratospheric water vapour trends derived from merged satellite data, *Nature Geoscience*, *7*, 768–776, doi:10.1038/NGEO2236.

Holton, J. R. (1992), *An Introduction to Dynamic Meteorology*, Academic Press, London.

Holton, J. R., P. Haynes, M. E. McIntyre, A. R. Douglass, R. B. Rood, and L. Pf ster (1995), Stratosphere-troposphere exchange, *Rev. Geophys.*, *33*, 403–439.

Homeyer, C. R., and K. P. Bowman (2012), Rossby wave breaking and transport between the tropics and extratropics above the subtropical jet, *J. Atmos. Sci.*, *70*, 607–626.

Hoor, P., C. Gurk, D. Brunner, M. I. Hegglin, H. Wernli, and H. Fischer (2004), Seasonality and extent of extratropical TST derived from in-situ CO measurements during SPURT, *Atmos. Chem. Phys.*, *4*, 1427–1442.

James, R., and B. Legras (2009), Mixing processes and exchanges in the tropical and the subtropical UT/LS, *Atmos. Chem. Phys.*, *9*, 25–38.

Kantz, H., and T. Schreiber (2004), *Nonlinear Time Series Analysis*, Cambridge University Press, Cambridge.

Kasahara, A. (1974), Various vertical coordinate systems used for numerical weather prediction, *Mon. Wea. Rev.*, *102*, 509–522.

Konopka, P. (1995), Analytical Gaussian solutions for anisotropic diffusion in a linear shear f ow, *J Non Equilib Thermodyn*, *20*, 78–91.

Konopka, P., and L. L. Pan (2012), On the mixing-driven formation of the Extratropical Transition Layer (ExTL), *J. Geophys. Res.*, *117*, D18301, doi:10.1029/2012JD017876.

Konopka, P., J.-U. Grooß, S. Bausch, R. Müller, D. S. McKenna, O. Morgenstern, and Y. Orsolini (2003a), Dynamics and chemistry of vortex remnants in late Arctic spring 1997 and 2000: Simulations with the Chemical Lagrangian Model of the Stratosphere (CLaMS), *Atmos. Chem. Phys.*, *3*, 839–849.

Konopka, P., J. U. Grooß, G. Günther, D. S. McKenna, R. Müller, J. W. Elkins, D. Fahey, and P. Popp (2003b), Weak impact of mixing on chlorine deactivation during SOLVE/THESEO2000: Lagrangian modeling (CLaMS) versus ER-2 in situ observations., *J. Geophys. Res.*, *108*, 8324, doi:10.1029/2001JD000876.

Konopka, P., J.-U. Grooß, K. W. Hoppel, H.-M. Steinhorst, and R. Müller (2005a), Mixing and chemical ozone loss during and after the Antarctic polar vortex major warming in September 2002, *J. Atmos. Sci.*, *62*(3), 848–859.

Konopka, P., G. Günther, D. S. McKenna, R. Müller, D. Offermann, R. Spang, and M. Riese (2005b), How homogeneous and isotropic is stratospheric mixing? Comparison of CRISTA-1 observations with transport studies based on the Chemical Lagrangian Model of the Stratosphere (CLaMS), *Q. J. R. Meteorol. Soc.*, *131*(606), 565–579, doi:10.1256/qj.04.47.

Konopka, P., J.-U. Grooß, F. Plöger, and R. Müller (2009), Annual cycle of horizontal in-mixing into the lower tropical stratosphere, *J. Geophys. Res.*, *114*, D19111, doi: 10.1029/2009JD011955, warning: BibtexKey has changed!!

Konopka, P., J.-U. Grooß, G. Günther, F. Ploeger, R. Pommrich, R. Müller, and N. Livesey (2010), Annual cycle of ozone at and above the tropical tropopause: observations versus simulations with the Chemical Lagrangian Model of the Stratosphere (CLaMS), *Atmos. Chem. Phys.*, *10*(1), 121–132, doi:10.5194/acp-10-121-2010, warning: BibtexKey has changed!!

Konopka, P., F. Ploeger, and R. Müller (2012), Entropy- and static stability-based Lagrangian model grids, in *Geophysical Monograph Series: Lagrangian Modeling of the Atmosphere*, vol. 200, edited by J. Lin, pp. 99–109, American Geophysical Union, doi: 10.1029/2012GM001253.

Konopka, P., F. Ploeger, M. Tao, T. Birner, and M. Riese (2015), Hemispheric asymmetries and seasonality of mean age of air in the lower stratosphere: Deep versus shallow branch of the brewer-dobson circulation, *J. Geophys. Res.*, *120*(5), 2053–2066, doi:10.1002/2014JD022429.

Konopka, P., et al. (2004), Mixing and ozone loss in the 1999-2000 Arctic vortex: Simulations with the 3-dimensional Chemical Lagrangian Model of the Stratosphere (CLaMS), *J. Geophys. Res.*, *109*, D02315, doi:10.1029/2003JD003792.

Konopka, P., et al. (2007), Contribution of mixing to upward transport across the tropical tropopause layer (TTL), *Atmos. Chem. Phys.*, *7*(12), 3285–3308.

Kunz, A., P. Konopka, R. Müller, L. L. Pan, C. Schiller, and F. Rohrer (2009), High static stability in the mixing layer above the extratropical tropopause, *J. Geophys. Res.*, *114*, D16305, doi: 10.1029/2009JD011840.

Lauritzen, P. H., P. A. Ullrich, and R. D. Nair (2011), *Atmospheric transport schemes: desirable properties and a semi-Lagrangian view on finite-volume discretizations*, pp. 185–250, Springer.

Legras, B., I. Pisso, G. Berthet, and F. Lefevre (2005), Variability of the lagrangian turbulent diffusion in the lower stratosphere, *Atmos. Chem. Phys.*, *5*, 1605–1622.

Lin, J., D. Brunner, C. Gerbig, A. Stohl, A. Luhar, and P. Webley (Eds.) (2013), *Lagrangian Modeling of the Atmosphere*, vol. 200, American Geophysical Union, Washington, DC.

Lin, S.-J., and R. B. Rood (1996), Multidimensional flux-form semi-lagrangian transport schemes, *Mon. Wea. Rev.*, *124*.

Lindzen, R. S., and M. S. Fox-Rabinovitz (1989), Consistent vertical and horizontal resolution, *Mon. Wea. Rev.*, *117*, 2575 – 2583.

Lyubarski, G. Y. (1960), *The Application of Group Theory in Physics*, Pergamon Press, Oxford.

Mahowald, N. M., R. A. Plumb, P. J. Rasch, J. del Corral, and F. Sassi (2002), Stratospheric transport in a three-dimensional isentropic coordinate model, *J. Geophys. Res.*, *107*(D15), 4254, doi:10.1029/2001JD001313.

Matsuno, T. (1971), A dynamical model of the stratospheric sudden warming, *J. Atmos. Sci.*, *28*(8), 1479–1494.

McKenna, D. S., P. Konopka, J.-U. Grooß, G. Günther, R. Müller, R. Spang, D. Offermann, and Y. Orsolini (2002), A new Chemical Lagrangian Model of the Stratosphere (CLaMS): 1. Formulation of advection and mixing, *J. Geophys. Res.*, *107*(D16), 4309, doi: 10.1029/2000JD000114.

Mote, P. W., et al. (1996), An atmospheric tape recorder: The imprint of tropical tropopause temperatures on stratospheric water vapor, *J. Geophys. Res.*, *101*(D2), 3989 – 4006.

Onsager, L. (1931), Reciprocal Relations in Irreversible Processes. I, *Phys. Rev.*, *37*, 405–426.

Ott, E. (1993), *Chaos in dynamical systems*, Cambridge University Press, Cambridge.

Pan, L. L., P. Konopka, and E. V. Browell (2006), Observations and model simulations of mixing near the extratropical tropopause, *J. Geophys. Res.*, *111*(D05106), D05106, doi: 10.1029/2005JD006480.

Pan, L. L., et al. (2007), Chemical behavior of the tropopause observed during the stratosphere-troposphere analyses of regional transport experiment, *J. Geophys. Res.*, *112*(D18110), doi: 10.1029/2007JD008645.

Pan, L. L., et al. (2009), Tropospheric intrusions associated with the secondary tropopause, *J. Geophys. Res.*, *114*(D10302), D10302, doi:10.1029/2008JD011374.

Pan, L. L., et al. (2010), The Stratosphere-Troposphere Analyses of Regional Transport 2008 (START08) Experiment, *Bull. Am. Meteorol. Soc.*, *91*, 327–342.

Park, M., W. J. Randel, L. K. Emmons, P. F. Bernath, K. A. Walker, and C. D. Boone (2008), Chemical isolation in the Asian monsoon anticyclone observed in Atmospheric Chemistry Experiment (ACE-FTS) data, *Atmos. Chem. Phys.*, *8*(3), 757–764.

Perko, L. (1996), *Differential equations and dynamical systems*, New-York, Springer.

Pierrehumbert, R. T., and H. Yang (1993), Global chaotic mixing on isentropic surfaces, *J. Atmos. Sci.*, *50*, 2462–2480.

Pisso, I., and B. Legras (2008), Turbulent vertical diffusivity in the sub-tropical stratosphere, *Atmos. Chem. Phys.*, *8*, 697–707.

Ploeger, F., P. Konopka, G. Günther, J.-U. Grooß, and R. Müller (2010), Impact of the vertical velocity scheme on modeling transport across the tropical tropopause layer, *J. Geophys. Res.*, *115*, D03301, doi:10.1029/2009JD012023.

Ploeger, F., et al. (2011), Insight from ozone and water vapour on transport in the tropical tropopause layer (TTL), *Atmos. Chem. Phys.*, *11*, 407–419, doi:10.5194/acp-11-407-2011.

Ploeger, F., et al. (2012), Horizontal transport affecting trace gas seasonality in the Tropical Tropopause Layer (TTL), *J. Geophys. Res.*, *117*, D09303, doi:10.1029/2011JD017267, warning: BibtexKey has changed!!

Plumb, R. A. (1996), A "tropical pipe" model of stratospheric transport, *J. Geophys. Res.*, *101*, 3957–3972.

Polvani, L. M., and J. G. Esler (2007), Transpotr and mixing of chemical air masses in idealized baroclinic life cycles, *J. Geophys. Res.*, *112*, 1–20.

Pommrich, R., et al. (2014), Tropical troposphere to stratosphere transport of carbon monoxide and long-lived trace species in the chemical lagrangian model of the stratosphere (clams), *Geoscientif c Model Development*, *7*(6), 2895–2916, doi:10.5194/gmd-7-2895-2014.

Preparata, F. P., and M. Shamos (1985), *Computational Geometry. An Introduction*, Springer-Verlag.

Randel, W., and E. Jensen (2013), Physical processes in the tropical tropopause layer and their role in a changing climate, *Nature Geoscience*, *6*, 169–176, doi:10.1038/ngeo1733.

Randel, W. J., and M. Park (2006), Deep convective inf uence on the Asian summer monsoon anticyclone and associated tracer variability observed with Atmospheric Infrared Sounder (AIRS), *J. Geophys. Res.*, *111*, D12314, doi:10.1029/2005JD006490.

Randel, W. J., R. R. Garcia, and F. Wu (2002), Time-dependent upwelling in the tropical lower stratosphere estimated from the zonal-mean momentum budget, *J. Atmos. Sci.*, *59*, 2141–2152.

Randel, W. J., F. Wu, S. J. Oltmans, K. Rosenlof, and G. E. Nodoluha (2004), Interannual changes of stratospheric water vapor and correlations with tropical tropopause temperatures, *J. Atmos. Sci.*, *61*, 2133–2148.

Randel, W. J., M. Park, F. Wu, and N. Livesey (2007a), A large annual cycle in ozone above the tropical tropopause linked to the Brewer-Dobson circulation, *J. Atmos. Sci.*, *64*, 4479–4488.

Randel, W. J., F. Wu, and P. Forster (2007b), The extratropical tropopause inversion layer: Global observations with GPS data, and a radiative forcing mechanism, *J. Atmos. Sci.*, *64*, 4489–4496, doi:10.1175/2007JAS2412.1.

Randel, W. J., M. Park, L. Emmons, D. Kinnison, P. Bernath, K. A. Walker, C. Boone, and H. Pumphrey (2010), Asian monsoon transport of pollution to the stratosphere, *Science*, *328*(5978), 611–613, doi:10.1126/science.1182274.

Reithmeier, C., and R. Sausen (2000), ATTILA - Atmospheric Tracer Transport in a Lagrangian Model, *Tech. rep.*, Institut für Physik der Atmosphäre, DLR-Oberpfaffenhofen, 82234 Wessling, Germany.

Riese, M., F. Ploeger, A. Rap, B. Vogel, P. Konopka, M. Dameris, and P. Forster (2012), Impact of uncertainties in atmospheric mixing on simulated UTLS composition and related radiative effects, *J. Geophys. Res.*, *117*, D16305, doi:10.1029/2012JD017751.

Rood, R. B. (1987), Numerical advection algorithms and their role in atmospheric transport and chemistry models, *Rev. Geophys.*, *25*(1), 71–100.

Satoh, M. (2014), *Atmospheric Circulation Dynamics and General Circulation Models*, Springer Praxis Books, Chichester, UK.

Schlager, H., et al. (1997), In situ observations of aircraft emissions signatures in the north atlantic f ight corridor, *J. Geophys. Res.*, *102*, 10,739–10,750.

Schoeberl, M. R., and A. R. Douglass (2010), Trace gas transport in the stratosphere: Diagnostic tools and techniques, in *The Stratosphere: Dynamics, Transport and Chemistry*, edited by L. M. Polvani, A. H. Sobel, and D. W. Waugh, pp. 137–156.

Schoeberl, M. R., A. R. Douglass, Z. X. Zhu, and S. Pawson (2003), A comparison of the lower stratospheric age spectra derived from a general circulation model and two data assimilation systems, *J. Geophys. Res.*, *108*(D3), 4113, doi:10.1029/2002JD002652.

Schoeberl, M. R., B. Duncan, A. R. Douglass, J. Waters, N. J. Livesey, W. Read, and M. Filipiak (2006), The carbon monoxide tape recorder, *Geophys. Res. Lett.*, *33*(12), L12811, doi: 10.1029/2006GL026178.

Schröter, J. (1995), The microscopic background of thermodynamics, *J Non Equilib Thermodyn*, *20*, 315–326.

Schumann, U., P. Konopka, R. Baumann, R. Busen, T. Gerz, H. Schlager, P. Schulte, and H. Volkert (1995), Estimation of diffusion parameters of aircraft exhaust plumes near the tropopause from nitric oxide and turbulence measurements, *J. Geophys. Res.*, *100*, 14,147–14,162.

Simmons, A., S. Uppala, Dee, and D. Kobayashi (2006), ERA-Interim: New ECMWF reanalysis products from 1989 onwards, *ECMWF Newsletter*, *110*, 25–35.

Smagorinsky, J. (1963), General circulation experiments with the primitive equations: I. the basic experiment, *Mon. Wea. Rev.*, *91*, 99–164.

Smolarkiewicz, P. K., and J. A. Pudykiewicz (1992), A class of semi-Lagrangian approximations for f uids, *J. Atmos. Sci.*, *49*, 2082–2096.

Solomon, S., D. Qin, M. Manning, M. Marquis, K. Averyt, M. M. B. Tignor, H. L. Miller, and Z. Chen (Eds.) (2007), *Climate Change 2007: The Physical Science Basis. Contribution of Working Group I to the Fourth Assessment Report of the Intergovernmental Panel on Climate Change*, 996 pp., Cambridge University Press, Cambridge, UK, and New York, NY, USA.

Solomon, S., K. Rosenlof, R. Portmann, J. Daniel, S. Davis, T. Sanford, and G.-K. Plattner (2010), Contributions of stratospheric water vapor to decadal changes in the rate of global warming, *Science*, *327*, 1219–1223, doi:10.1126/science.1182488.

Stevenson et al., W. J. (2006), Multimodel ensemble simulations of present-day and near-future tropospheric ozone, *J. Geophys. Res.*, *111*, doi:10.1029/2005JD006338.

Stocker, T. F., et al. (Eds.) (2013), *Climate Change 2013: The Physical Science Basis. Contribution of Working Group I to the Fifth Assessment Report of the Intergovernmental Panel on Climate Change*, 1535 pp., Cambridge University Press, Cambridge, UK and New York, NY, USA.

Stohl, A. (1998), Computations, accuracy and applications of trajectories – a review and bibliography, *Atmos. Environ.*, *32*(6), 947–966.

Tao, M., P. Konopka, F. Ploeger, J.-U. Grooß, R. Müller, C. Volk, K. Walker, and M. Riese (2015a), Impact of the 2009 major stratospheric sudden warming on the composition of the stratosphere, *Atmos. Chem. Phys.*, pp. 8695–8715, doi:10.5194/acp-15-8695-2015.

Tao, M., P. Konopka, F. Ploeger, M. Riese, R. Müller, and C. Volk (2015b), Impact of stratospheric major warmings and the quasi-biennial oscillation on the variability of stratospheric water vapor, *Geophys. Res. Lett.*, *42*(11), 4599–4607, doi:10.1002/2015GL064443.

Thuburn, J. (2008), Some conservation issues for the dynamical cores of NWP and climate models, *J. Comput. Phys.*, *227*, 3715–3730.

Tuck, A. F. (1986), Depletion of Antarctic ozone, *Nature*, *321*, 729–730.

Turner, J. S. (1973), *Buoyancy Effects in Fluids*, Cambridge University Press.

Uppala, S., S. Dee, S. Kobayashi, P. Berrisford, and A. Simmons (2008), Towards a climate data assimilation system: status update of ERA-Interim, *ECMWF Newsletter*, *115*, 12–18.

Urban, J., S. Lossow, G. Stiller, and W. Read (2014), Another drop in water vapor, *Eos, Transactions American Geophysical Union*, *95*(27), 245–246.

Vallis, G. K. (2006), *Atmospheric and oceanic f uid dynamics*, Cambridge University Press.

Vogel, B., et al. (2011), Transport pathways and signatures of mixing in the extratropical tropopause region derived from Lagrangian model simulations, *J. Geophys. Res.*, *116*, D05306, doi:10.1029/2010JD014876.

Wang, Y., P. Konopka, Y. Liu, H. Chen, R. Müller, F. Ploeger, M. Riese, Z. Cai, and D. Lü (2012), Tropospheric ozone trend over Beijing from 2002–2010: Ozonesonde measurements and modeling analysis, *Atmos. Chem. Phys.*, *12*(18), 8389–8399, doi:10.5194/acp-12-8389-2012, warning: BibtexKey has changed!!

Waugh, D. W., et al. (1997), Mixing of polar vortex air into middle latitudes as revealed by tracer-tracer scatterplots, *J. Geophys. Res.*, *102*, 13,119–13,134.

Wirth, V. (2003), Static stability in the extratropical tropopause region, *J. Atmos. Sci.*, *60*, 1395–1409.

Wirth, V. (2004), A dynamical mechanism for tropopause sharpening, *Meteorol. Z.*, *15*, 477–484.

Wirth, V., and T. Szabo (2007), Sharpness of the extratropical tropopause in baroclinic life cycle experiments, *Geophys. Res. Lett.*, *34*, L02809, doi:10.1029/2006GL028369.

WMO (2003), *Scientif c assessment of ozone depletion: 2002*, Global Ozone Research and Monitoring Project–Report No. 47, Geneva, Switzerland.

Wohltmann, I., and M. Rex (2008), Improvement of vertical and residual velocities in pressure or hybrid sigma-pressure coordinates in analysis data in the stratosphere, *Atmos. Chem. Phys.*, *8*, 265–272.

Wohltmann, I., and M. Rex (2009), The lagrangian chemistry and transport model atlas: validation of advective transport and mixing, *Geosci. Model Dev.*, *2*(2), 153–173, doi:10.5194/gmd-2-153-2009.

Woodman, R. F., and P. K. Rastogi (1984), Evaluation of effective eddy diffusivity coeff cients using radar observations of turbulence in the stratosphere, *Geophys. Res. Lett.*, *211*, 243–246.

Yang, Q., Q. Fu, J. Austin, A. Gettelman, F. Li, and H. Vömel (2008), Observationally derived and general circulation model simulated tropical stratospheric upward mass f uxes, *J. Geophys. Res.*, *113*, doi:10.1029/2008JD009945.

Acknowledgements

First of all, I would like to thank Volkmar Wirth, who gave me the opportunity to undertake my *Habilitation* at the University of Mainz. He and Peter Hoor are the mentors of this work and during the last four years they offered me support and a lot of excellent advice on preparing good lectures for students.
This work would not have been possible without the support of my current employer, Forschungszentrum Jülich. My thanks go to Martin Riese, the director of my current Institute of Energy and Climate Research Stratosphere (IEK-7), but most of all to Rolf Müller. During the last 18 years, he has not only been my immediate superior but also my most important scientif c partner.
This work also would not have been possible without the support of the team, the CLaMS group, its permanent staff: Verena Alishahi, Nicole Thomas, Bärbel Vogel, Jens-Uwe Grooß, Gebhard Günther and Reinhold Spang. I would especially like to thank Nicole Thomas, whose work forms the backbone of my scientif c activities.
During the last 10 years, many talented young scientists encouraged me to complete this work. My gratitude is due in particular to Felix Plöger, Mengchu Tao, Anne Kunz, Marc von Hobe, Yong Wang, Charlotte Hoppe, Ines Tritscher, Xiaolu Yan and Mohamadou Diallo. Especially, the scientif c discussions with Felix Plöger were extremely important for me during the last few years.
Finally, the most important external scientif c support came from the Atmospheric Chemistry Division at NCAR in Boulder, USA, especially from Bill Randel and most of all from Laura Pan, who deserves special credit.
I would like to emphasize the good working atmosphere at my institute, which gave me a lot of strength and energy. Last but not least, I would also like to mention Danny McKenna, who initiated the theoretical studies based on Lagrangian transport in Jülich and who aroused my interest in this topic.

Band / Volume 386
IEK-3 Report 2017
Sector Coupling –
Research for an Integrated Energy System
(2017), 175 pp
ISBN: 978-3-95806-258-0

Band / Volume 387
Photochemistry of Highly Oxidized Multifunctional Organic Molecules: a Chamber Study
L. I. M. Pullinen (2017), II, 96, xviii pp
ISBN: 978-3-95806-260-3

Band / Volume 388
Poröse Transportschichten für die Polymerelektrolytmembran-Wasserelektrolyse
M. Höh (2017), VI, 186 pp
ISBN: 978-3-95806-262-7

Band / Volume 389
Modelling of High Temperature Polymer Electrolyte Fuel Cells
Q. Cao (2017), 173 pp
ISBN: 978-3-95806-263-4

Band / Volume 390
Potential use of nitrification inhibitors for mitigating N_2O emission from soils
D. Wu (2017), 206 pp
ISBN: 978-3-95806-264-1

Band / Volume 391
Mechanical Characterization of Solid Oxide Fuel Cells and Sealants
J. Wei (2017), II, 151 pp
ISBN: 978-3-95806-266-5

Band / Volume 392
Microcrystalline Silicon Carbide for Silicon Heterojunction Solar Cells
M. B. Pomaska (2017), 150 pp
ISBN: 978-3-95806-267-2

Band / Volume 393
Einfluss der Kristallisation auf das Fließverhalten oxidischer Schmelzen
S. Seebold (2017), 168 pp
ISBN: 978-3-95806-268-9

Band / Volume 394
Water vapour in the UTLS – Climatologies and Transport
P. R. Neis (2017), x, 124 pp
ISBN: 978-3-95806-269-6

Band / Volume 395
Neutronenaktivierungsanalyse mit gepulsten 14 MeV Neutronen zur Charakterisierung heterogener radioaktiver Abfälle
F. Mildenberger (2017), vi, 128 pp
ISBN: 978-3-95806-271-9

Band / Volume 396
Coupled biotic-abiotic mechanisms of nitrous oxide production in soils during nitrification involving the reactive intermediates hydroxylamine and nitrite
S. Liu (2017), xvii, 148 pp
ISBN: 978-3-95806-272-6

Band / Volume 397
Mixed-phase and ice cloud observations with NIXE-CAPS
A. Costa (2017), xviii, 117 pp
ISBN: 978-3-95806-273-3

Band / Volume 398
Deposition Mechanisms of Thermal Barrier Coatings (TBCs) Manufactured by Plasma Spray-Physical Vapor Deposition (PS-PVD)
W. He (2017), ix, 162 pp
ISBN: 978-3-95806-275-7

Band / Volume 399
Carbonyl Sulfide in the Stratosphere: airborne instrument development and satellite based data analysis
C. Kloss (2017), vi, 84, 1-14 pp
ISBN: 978-3-95806-276-4

Band / Volume 400
Lagrangian transport of trace gases in the upper troposphere and lower stratosphere (UTLS)
P. Konopka (2017), 70 pp
ISBN: 978-3-95806-279-5

Weitere ***Schriften des Verlags im Forschungszentrum Jülich*** unter
http://wwwzb1.fz-juelich.de/verlagextern1/index.asp

Energie & Umwelt /
Energy & Environment
Band / Volume 400
ISBN 978-3-95806-279-5